https://doi.org/10.1144/jgs2024-289 | Vol. 182 | 2025 | jgs2024-289

3D seismic characterization of magma plumbing components in the Tarim Large Igneous Province, north-central Tarim Basin, **NW China**



Xinyu Dong^{1,2}, Gary J. Hampson^{2*}, Craig Magee³, Lidia Lonergan² and Yanghua Wang^{1,2}

- ¹ Resource Geophysics Academy, Imperial College London, South Kensington Campus, London SW7 2BP, UK
- ² Department of Earth Science and Engineering, Imperial College London, South Kensington Campus, London SW7 2AZ, UK
- ³ School of Earth and Environment, University of Leeds, Woodhouse, Leeds LS2 9JT, UK
- 6 GJH, 0000-0003-2047-8469; CM, 0000-0001-9836-2365; LL, 0000-0001-9858-3029; YW, 0000-0002-1044-4348

Present addresses: XD, Geophysical Research Institute, Sinopec, Jiangning, Nanjing, 211103, China

Abstract: Linkages between upper-crustal intrusive and extrusive components of magma plumbing systems in Large Igneous Provinces (LIPs) are challenging to reconstruct. We used 3D seismic reflection and borehole data to characterize these components and their relationships in the Permian LIP of the north-central Tarim Basin in China. A connected network of areally extensive (from 10 to >115 km²), saucer-shaped, gabbro and diabase sills cuts across 2 km of strata and fed extrusive basalt lava flows. These basalts cap a high-volume (>250 km³) volcaniclastic mass transport complex and an underlying set of steeply dipping (5°) volcanic lastic clinoforms, indicating substantial remobilization and reworking of volcanic debris. The clinoform set records progradation of an arcuate shoreline composed of dacite tuff and tuffaceous sediment. The mass transport complex comprises dacite and basalt megaclasts (up to 4 km³), basaltic tuff, and volcaniclastic sediment. Its base is marked by large polygonal ridges and depressions (up to 1000 m in lateral spacing and 40 m in relief), indicating water escape driven by loading and compaction. Older sills variably cut across and are cut by long-lived strike-slip faults, while the youngest sill intrudes the volcaniclastic clinoform set and is associated with forced folding and subsequent onlap of strata containing basalt

Supplementary material: Four supplementary figures are available at https://doi.org/10.6084/m9.figshare.c.7895831

Received 18 December 2024; revised 18 April 2025; accepted 2 June 2025

Large Igneous Provinces (LIPs) are characterized by extensive subsurface networks of dyke and sill intrusions, and thick layers of extruded flood basaltic lavas (e.g. Coffin and Eldholm 1994; Gao et al. 2017; Srivastava et al. 2022). Understanding the dimensions, distributions and relationships between these intrusive and extrusive components constrains the magma transport pathways and their spatio-temporal evolution in a LIP, which can, in turn, facilitate analysis of magma evolution and related geodynamic processes. Furthermore, LIPs mark key phases in basin evolution and may significantly influence basin thermal histories and fluid-flow pathways, including hydrocarbon migration (e.g. Holford et al. 2013; Eide et al. 2017; Schofield et al. 2017). Although numerous studies have used seismic reflection and well-log data to characterize intrusive and extrusive igneous products and processes in volcanic regions (e.g. Smallwood and Maresh 2002; Planke et al. 2005, 2017; Cartwright and Hansen 2006; Schofield et al. 2017; Quirie et al. 2019; Walker et al. 2022), it remains challenging to link intrusive and extrusive components of magma plumbing systems in LIPs, due to their large areal extent and incomplete preservation in areas of uplift and denudation (e.g. Ernst et al. 2019; Magee et al. 2019; Srivastava et al. 2022). In this paper, we use 3D seismic reflection and well-log data from the Permian LIP in the Tarim Basin, NW China to characterize upper-crustal intrusive and extrusive components and, for the first time, their linkage in its magma plumbing system.

Current understanding of the magma plumbing system of the Tarim LIP is mainly based on either intrusive or extrusive igneous

rocks imaged in seismic reflection data and penetrated by boreholes from the Tabei, Tazhong and Shuntuoguole Low uplifts of the central Tarim Basin (e.g. Wang et al. 2015; Yang et al. 2016; Gao et al. 2017; Yao et al. 2018; Ji et al. 2020; Xiao et al. 2020; Liu et al. 2022; Niu et al. 2024; Yao 2024), and on petrological and geochemical investigations of igneous rocks that crop out along the northwestern and southwestern margins of the basin (Fig. 1a) (e.g. Zhou et al. 2009; Shangguan et al. 2012; Z. Li et al. 2017). Many of these studies focused on the development of secondary porosity in deeply buried carbonate reservoirs associated with the movement of deep hydrothermal fluids along faults and fracture zones, which is attributed to magmatic activity and the intrusion of dykes and sills (Lan et al. 2014; Xu et al. 2015). Recent hydrocarbon exploration in the Shunbei area of the Shuntuoguole Low Uplift, north-central Tarim Basin, has prompted several studies investigating intrusive igneous sills and their relationship with strike-slip faults (e.g. Deng et al. 2022; Liu et al. 2022; Niu et al. 2024). However, the relationship between extrusive and intrusive igneous rocks in this area, and in the Tarim Basin in general, has yet to be documented. More detailed investigations are necessary to elucidate the internal structure and the interrelationships of Permian extrusive and intrusive igneous rocks, and thereby to reconstruct the magma plumbing system within the Tarim LIP. To achieve this objective, this study utilized 3D seismic data calibrated with borehole data: (1) to document the internal character, geometry and distribution of Permian igneous rocks in the Shunbei area, north-central Tarim Basin; (2) to establish the relationship between intrusive dykes and

^{*}Correspondence: g.j.hampson@imperial.ac.uk

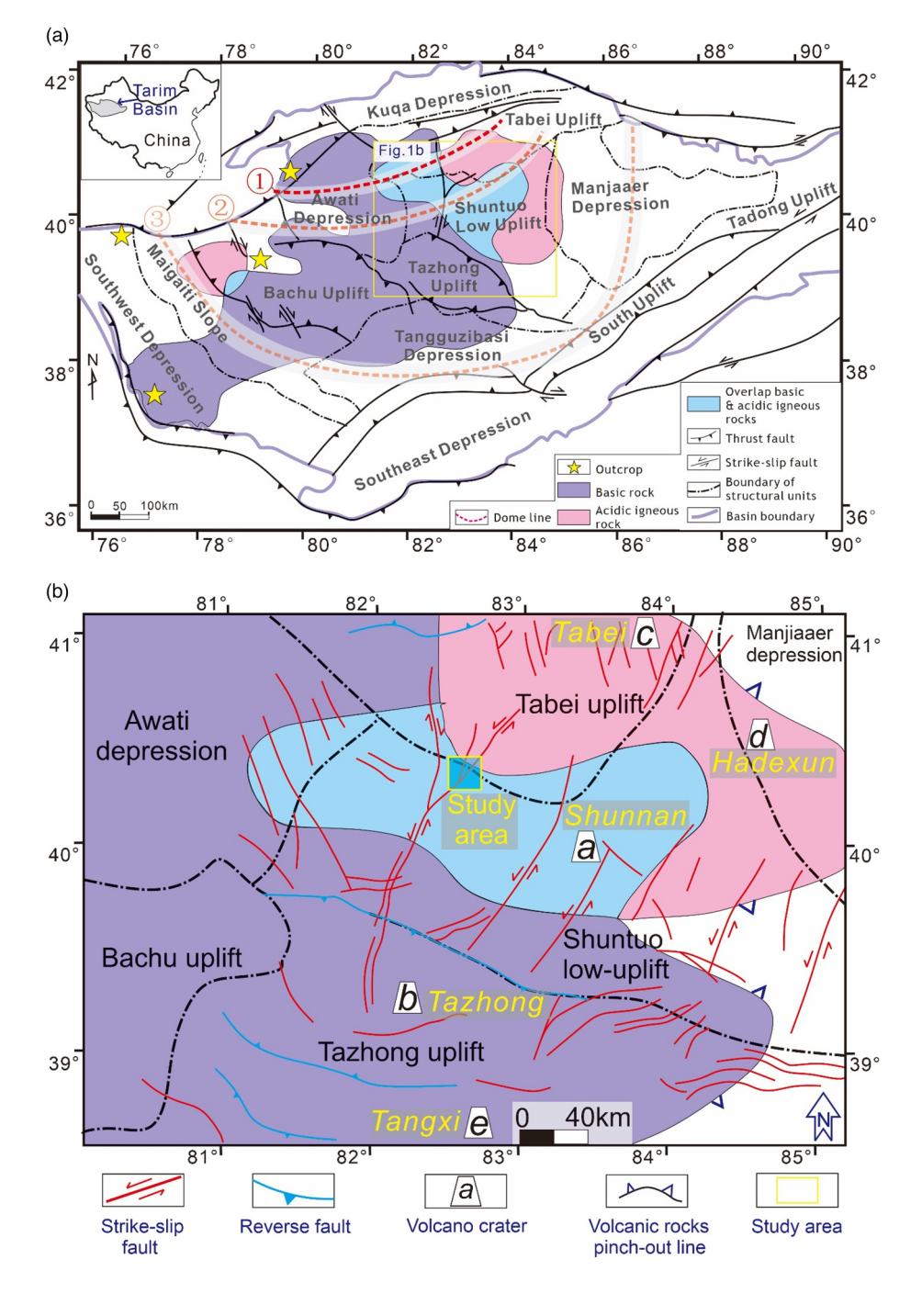


Fig. 1. (a) Map of the Tarim Basin showing tectonic elements and associated structural boundaries, the distribution of Permian igneous rocks, and domal uplift attributed to development of the Tarim LIP (uplift increases from red dashed line 3 to red dashed line 1). (b) Map of the central Tarim Basin showing faults and documented volcanic centres: 'a', Shunnan craters; 'b', Tazhong craters; 'c', Tabei craters; 'd', Hadexun craters; 'e', Tangxi craters. Source: (a) modified after Zhang et al. (2010), Yu et al. (2011), Yang et al. (2013), Li et al. (2014) and Deng et al. (2022); and (b) from Pu et al. (2012), Li et al. (2016), Yang et al. (2016) and Zhu and Zhang (2022).

sills and extrusive igneous rocks; and (3) to reconstruct the magma plumbing system.

Geological background

Tectonic setting of the Tarim Basin

The Tarim Basin, located in NW China, is bounded by the Tianshan Mountains in the north, the Altyn Mountains in the east and the Kunlun Mountains in the south, with an area of $c. 5.6 \times 10^5 \, \mathrm{km^2}$ and basin-fill strata up to 20 km thick (Fig. 1) (Lin *et al.* 2012). The basin has a complex evolutionary history, including Proterozoic—middle Silurian extension, late Silurian compression, Carboniferous—middle Triassic extension, late Triassic compression, Jurassic—Paleogene extension and Neogene compression (Lin *et al.* 2012; Wang *et al.* 2020). The basin is subdivided into 13 tectonic elements ('depressions' and 'uplifts') based on their stratal and structural characteristics (Fig. 1) (Deng *et al.* 2019). The basin

has pre-Sinian (Proterozoic) metamorphic basement, and the basin-fill strata consist of Sinian (late Precambrian)—Paleozoic marine carbonates, Mesozoic marine and continental siliciclastic strata, and Cenozoic continental siliciclastic strata (Fig. 2a) (Wang *et al.* 2020).

The Permian period marks the transition from marine to continental depositional environments in the Tarim Basin (Lin et al. 2012). Lower Permian strata consist of dolomite, sandstone and mudstone (Xu et al. 2017), while middle Permian strata comprise mafic and felsic igneous rocks, including intrusive diabase, effusive volcanic rocks (andesitic basalt, basalt and dacite) and volcaniclastic deposits (basalt tuff and dacite tuff) (Yang et al. 2016). Upper Permian strata primarily comprise argillaceous limestone (Fig. 2b) (Z. Li et al. 2017; Xiao et al. 2020). Magma differentiation resulted in the formation of extrusive and intrusive igneous rocks in the Tarim Basin (Ji et al. 2020).

Carboniferous—lower Triassic strata of the study area are summarized in Figure 2b. Siliciclastic Carboniferous strata were deposited in an epicontinental marine environment (Li *et al.* 2022).

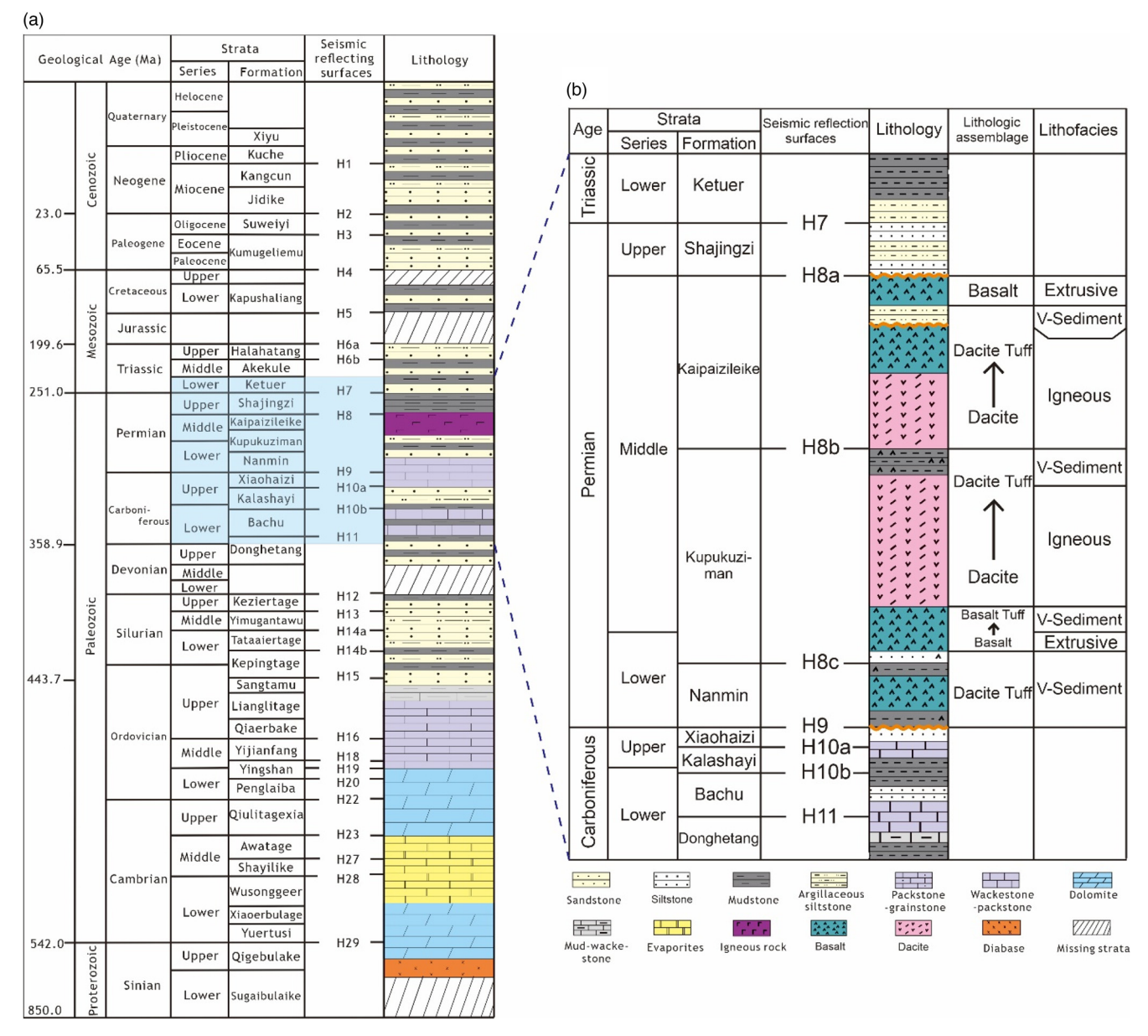


Fig. 2. (a) Stratigraphic chart of the Tarim Basin; and (b) stratigraphic column of Carboniferous–lower Triassic strata in the study area. Source: (a) modified after Deng et al. (2022) and Dong et al. (2024); and (b) modified after Hu (2019), Xiao et al. (2020) and Liu et al. (2022).

The contacts between Carboniferous and Permian strata and between Permian and Triassic strata in the central Tarim Basin are marked by unconformities resulting from tectonic uplift and erosion (Li *et al.* 2014). Following a late Permian depositional hiatus, Triassic strata consist of lithic sandstone and gravel, silty mudstone, and mudstone with a thickness of *c.* 800 m (Chen and Xu 2021). Subsequently, the study area experienced further uplift and erosion due to Jurassic collision between the Qiangtang and Tarim terrains (Li *et al.* 2022).

Deep-seated strike-slip faults are developed in the pre-Sinian basement–Cenozoic strata of the central and northern Tarim Basin (Fig. 1). These strike-slip faults initiated in the Ordovician and subsequently underwent multiple phases of mid-Paleozoic–Mesozoic movement (Tang *et al.* 2014; Sun *et al.* 2021), while their distribution reflects the geometry of tectonic elements in the basin interior (Fig. 1a) (Tang *et al.* 2014). Some studies propose that magma migrated along these deep-seated strike-slip faults during the Permian (e.g. Ma *et al.* 2013; Hu 2019). Thrust faults around the basin periphery developed (Fig. 1a) in the Neogene (Lin *et al.* 2012; Tang *et al.* 2014).

Permian igneous rocks in the Tarim Basin

The Tarim LIP developed within the Tarim Basin, spans a present-day area of $c.\ 2.6 \times 10^5\ \mathrm{km^2}$ and contains a succession of igneous rocks up to 800 m thick (Gao *et al.* 2017), mainly distributed in the western part of the Tarim Basin (Fig. 1). The suite of igneous rocks in the Tarim LIP include ultramafic/mafic—intermediate/felsic intrusions, continental flood basalts, andesite, diabase and mafic—felsic volcanic tuff (Yang *et al.* 2013; Xu *et al.* 2015; Gao *et al.* 2017; Xiao *et al.* 2020). The lower—middle Permian Kupukuziman Formation and the middle Permian Kaipaizileike Formation, exposed along the western and northern margins of the Tarim Basin, consist mainly of basalt and felsic rocks (Fig. 2) (Li *et al.* 2011). The Tarim LIP formed primarily through two phases of volcanic activity: intermediate—mafic and felsic extrusive volcanism at $c.\ 290$ –280 Ma; and intermediate—mafic intrusive volcanism at $c.\ 280$ –270 Ma (Z. Li *et al.* 2011, 2017; Yang *et al.* 2013).

Mantle plume and continental rifting models have been proposed as potential formation mechanisms for the Tarim LIP. The northern Tarim Basin experienced significant crustal uplift and erosion 4

during the late Carboniferous (e.g. Fig. 1a), followed by minor subsidence and pre-eruption deposition during the early Permian. This period was characterized by a persistent dome geomorphology, which is interpreted to have formed above a mantle plume (Chen et al. 2006; Li et al. 2014; Ji et al. 2020). In addition, rare earthelement (REE) and trace-element analyses suggest a potential association between the Tarim LIP and mantle plume activity (Yang et al. 2013; Wei et al. 2014). Alternatively, a continental rifting origin is supported by the eruption of olivine tholeitic basalt lava flows, of similar composition to ocean island basalts (OIBs), in the late Permian (Wang and Liu 1991; Xu et al. 2014, 2015) and the rare occurrence of intermediate volcanic rocks (Liu et al. 2011).

Data and methodology

Our study area is located within the Shuntuoguole Low Uplift in the central Tarim Basin (Fig. 1b) (Dong et al. 2024). This investigation employed pre-stack, full-fold, isotropic, time-migrated 3D seismic reflection data, acquired in 2019, within the study area, covering c. 750 km² (Fig. 3a) and extending for up to 6 s of two-way travel time (TWT) in the time domain. The study area is covered by aeolian dunes that are 10-150 m high. These surficial sediments and the Permian extrusive and intrusive igneous rocks in deeper strata lead to significant energy absorption and attenuation during seismic wave propagation. Small- to medium-sized bins, long arrays, wide azimuths and high coverage were used during seismic acquisition to address the resulting low signal-to-noise ratio, low dominant frequency, narrow effective frequency bandwidth and seismic-wave interference (Li et al. 2020; Qi 2023). A static correction constrained by uphole tomography, signal enhancement technologies for weak diffraction and scattered waves, and angle-domain migration were applied during data processing (Qi 2023). The processed 3D seismic reflection data have a vertical sampling interval of 2 ms (TWT), with both inlines (north-south direction) and crosslines (east-west direction), and a bin size of 25 m. The seismic data were zerophased and presented following the Society of Exploration Geophysicists (SEG) normal polarity convention, whereby a rise in acoustic impedance (hard kick) with depth is depicted as a peak (red reflection), and a decline in acoustic impedance (soft kick) with depth is portrayed as a trough (blue reflection).

Nine boreholes that penetrate Permian volcanic strata were used for lithological calibration of seismic data in this study (wells X-1, X-3, X-4, X-6, X-7, X-8, X-9, X-10 and X-11 in Fig. 3a). Both density (DEN) and P-wave sonic (AC) logs were available for eight wells, with only the AC log available for well X-3. Core samples, thin sections and geochemical analysis from the studied strata had been documented in nearby wells in the study area by Xiao *et al.* (2020), and the related well-log responses and seismic reflection patterns were utilized to calibrate these core-based interpretations with our dataset. These interpretations also refer to generic wireline-log responses (e.g. Rider and Kennedy 2011).

The vertical resolution of seismic data in the stratigraphic interval of interest was determined using an interval velocity of 4.4 km s⁻¹ (calculated from well X-4 at a depth of c. 5600 m: Fig. 4) and a dominant frequency of 25 Hz in the pre-stack reverse time migration (RTM) seismic data. These parameters indicate that a stratal thickness of c. 45 m can be fully resolved, assuming that the minimum resolution is a quarter of the wavelength (λ /4). Similarly, seismic resolution of the volcanic strata is c. 38 m, as determined from the dominant frequency of 26 Hz and average velocity of 4 km s⁻¹ (calculated from well X-10 at a depth of c. 4700 m: Fig. 4). Moreover, many sills in the study area are expressed as tuned reflection packages, where the reflections from their upper and lower boundaries coincide, making it difficult to constrain their thickness (Schofield et a. 2012b; Eide et a. 2018). The seismic reflection detection limit (visibility) (λ /32: Yilmaz 2001; Lebedeva-Ivanova

et al. 2018) of intrusive sills in this study was 17 m based on the dominant frequency of 22 Hz and the average velocity of 5.5 km s⁻¹ (calculated from well X-7, at a depth of c. 6800 m: Fig. 4), meaning that only sills with a thickness of more than 17 m could be identified. A horizontal detection capability of c. 60 m was indicated by the bin size of the seismic dataset $(25 \times 25 \text{ m})$, although the horizontal resolution may be less due to the influence of the Fresnel Zone.

A workflow integrating multiple interpretation methods to identify and classify igneous rocks was implemented, including: mapping key horizon surfaces; generating time-structure, timethickness (isochron) and seismic attribute maps in units defined by mapped surfaces; conducting seismic facies analysis in these units; calibrating seismic facies to lithology using well-log data and published core interpretations; and delineating sills based on their geometry. Igneous rocks typically exhibit a higher density than the surrounding host sedimentary rocks, resulting in a strong contrast in the acoustic impedance and correspondingly high seismic reflection amplitudes (e.g. Smallwood and Maresh 2002). In addition, sills typically terminate abruptly in the transverse direction (e.g. Ji et al. 2020). However, seismic reflections from steeply inclined sills or dykes may not be clear (Fig. 3b, c). In such cases, intrusions are mapped as subvertical zones characterized by narrow seismically opaque, chaotic or low-amplitude characteristics (Joppen and White 1990; Skogeid et al. 1992; Thomson 2007), and by the deformation of surrounding strata, such as forced folds (e.g. Magee et al. 2017; Tian et al. 2021) or peripheral faults (e.g. Liu et al. 2022).

Mapped stratigraphic units were correlated with well tops through well–seismic ties, which also provided constraints on the ages of the stratigraphic units. Fourteen mapped horizons were identified (Figs 2 and 3c), including, from shallowest to deepest, the tops of the upper Permian Shajingzi Formation (horizon H7), the middle Permian Kaipaizileike (horizon H8a) and Kupukuziman (horizon H8b) formations, the lower Permian Nanmin Formation (horizon H8c), the upper Carboniferous Xiaohaizi Formation (horizon H9), the lower–upper Carboniferous Kalashayi Formation (horizon H10a), the lower Carboniferous Bachu Formation (horizon H10b), the upper Devonian Donghetang Formation (horizon H11), the Silurian Keziertage (horizon H12), Yimugantawu (horizon H13) and Tataaiertage formations (horizon H14a), the lower Silurian–upper Ordovician Keziertage Formation (horizon H14b), and the upper Ordovician Sangtamu (horizon H15) and Qiaerbake (horizon H16) formations.

Attribute maps of the mapped horizons and volumes between mapped horizons, and seismic time–thickness (isochron) maps of volumes between mapped horizons, were generated for analysis. Three attributes were used: (1) the dip attribute, which measures the angle between the horizontal plane and the steepest direction of the mapped plane, and helps to identify folds and faults, even those with small displacements (Dalley *et al.* 1989); (2) the root mean square (RMS) amplitude, which measures the root mean squares of instantaneous trace samples over a specified window, and highlights changes in lithology, pore fluid type and/or fluid saturation; and (3) chaos, which describes the variability of the local seismic signal from a statistical analysis of dip and azimuth estimates, and which is useful for identifying faults and lithological discontinuities (Koson *et al.* 2013).

Results: seismic facies analysis

Seismic reflection continuity, amplitude, configuration and geometry were characterized in the studied strata. Table 1 summarizes the classification criteria for five seismic facies identified in this study: (1) High–Moderate Amplitude Chaotic (HMAC); (2) Inclined Moderate Amplitude Discontinuous (IMAD); (3) Low Amplitude Continuous (LAC); (4) High Amplitude Continuous (HAC) and (5) Very High Amplitude Continuous (VHAC) (Table 1). Seismic facies were calibrated to lithologies using wireline-log responses and

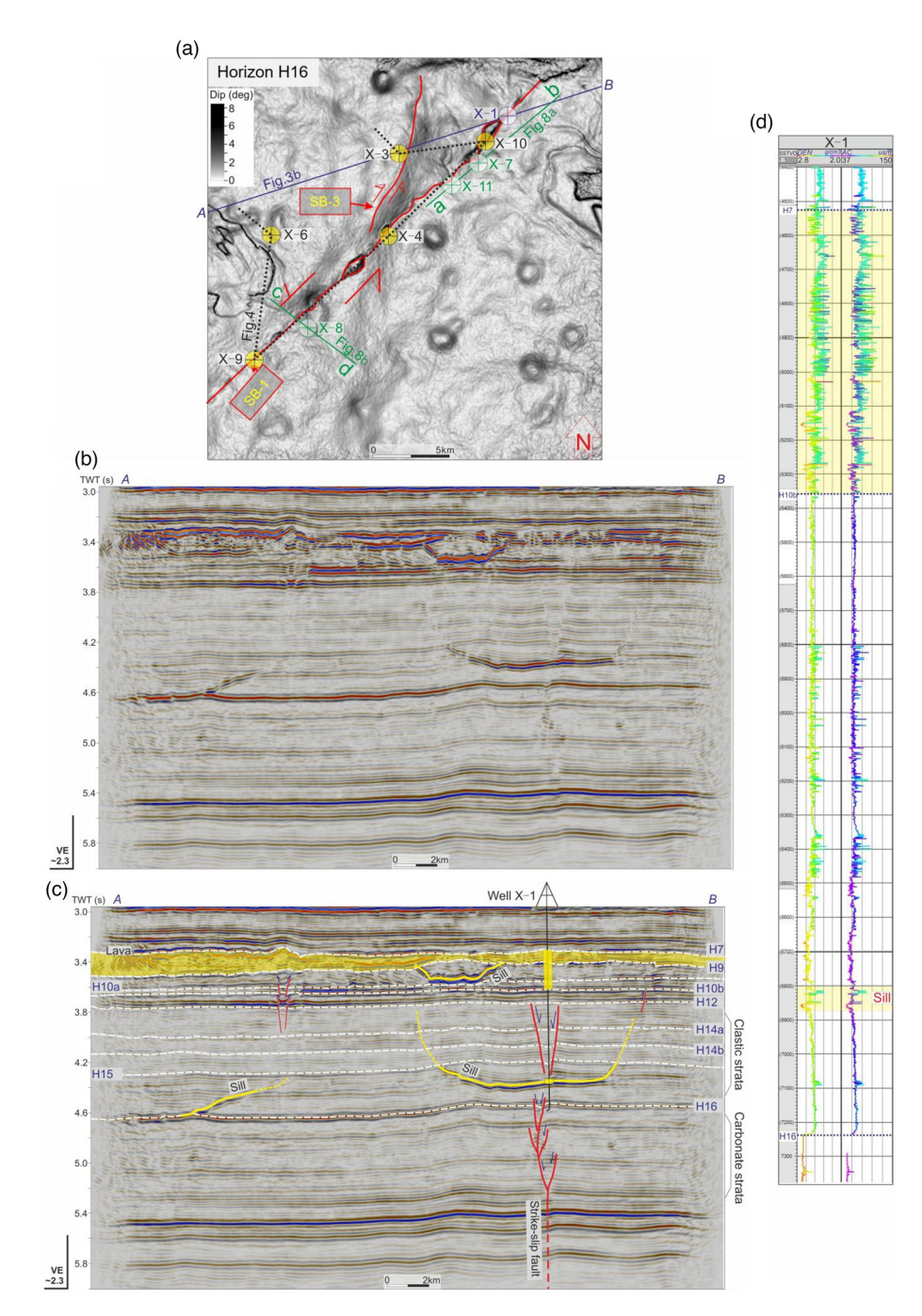


Fig. 3. (a) Dip attribute map of horizon H16 (Fig. 2) locating two strike-slip faults (SB-1 and SB-3), wells within the 3D seismic dataset, seismic cross-sections – (b), (c), and Figs 4 and 8a, b – and well correlation panel (Fig. 4). (b) Uninterpreted and (c) interpreted vertical seismic section across the seismic dataset, shown in (a). (d) Density and P-sonic logs of well X-1, see (a) and (c) for the locations. VE, vertical exaggeration.

published core samples (Xiao *et al.* 2020). Although the five seismic facies can generally be distinguished with a high degree of confidence, uncertainty in their identification arises from gradual transitions between reflection characteristics (e.g. between the LAC and HAC seismic facies) and tuning effects where lithological units thin and pinch out (e.g. at the lateral terminations of the VHAC seismic facies). Uncertainty in the lithological calibration is attributed to sparse well penetrations, non-unique combinations of wireline-log characteristics (density, sonic velocity) that control reflection amplitude and the small number of published core samples.

Seismic facies 1: High-Moderate Amplitude Chaotic (HMAC)

Description

Disrupted and hummocky, randomly distributed seismic reflectors, with moderate-high amplitudes, are apparent between horizons H7 and H9 in the seismic reflection profile (Fig. 4b, c), and constitute the High-Moderate Amplitude Chaotic (HMAC) seismic facies

(Table 1). The unit containing the HMAC seismic facies gradually thins from SW to NE, with thickness variations from 0.06 to 0.2 s TWT (Fig. 5a). In the northeastern part of the study area, overlying strata onlap this unit (Fig. 5c, d).

Calibration to wireline-log data

Three wells penetrate the HMAC seismic facies (wells X-9, X-4 and X-10: Fig. 4). The density (DEN) and P-wave sonic (AC) log responses in these wells show relatively uniform values of 2.55 g cm⁻³ (DEN) and 62 $\mu s/ft$ (AC) in the HMAC facies (4450–4700 m in X-9, 4500–4700 m in X-4 and 4520–4710 m in X-10: e.g. ® in Fig. 4a, c), although DEN values decrease to 2.42 g cm⁻³ and AC values increase to 55 $\mu s/ft$ (4620–4650 m in X-9, 4570–4630 m in X-4 and 4650–4660 m in X-10).

Interpretation

The configuration of reflectors in the unit of HMAC seismic facies contrasts with the continuous, sub-parallel to parallel geometry of



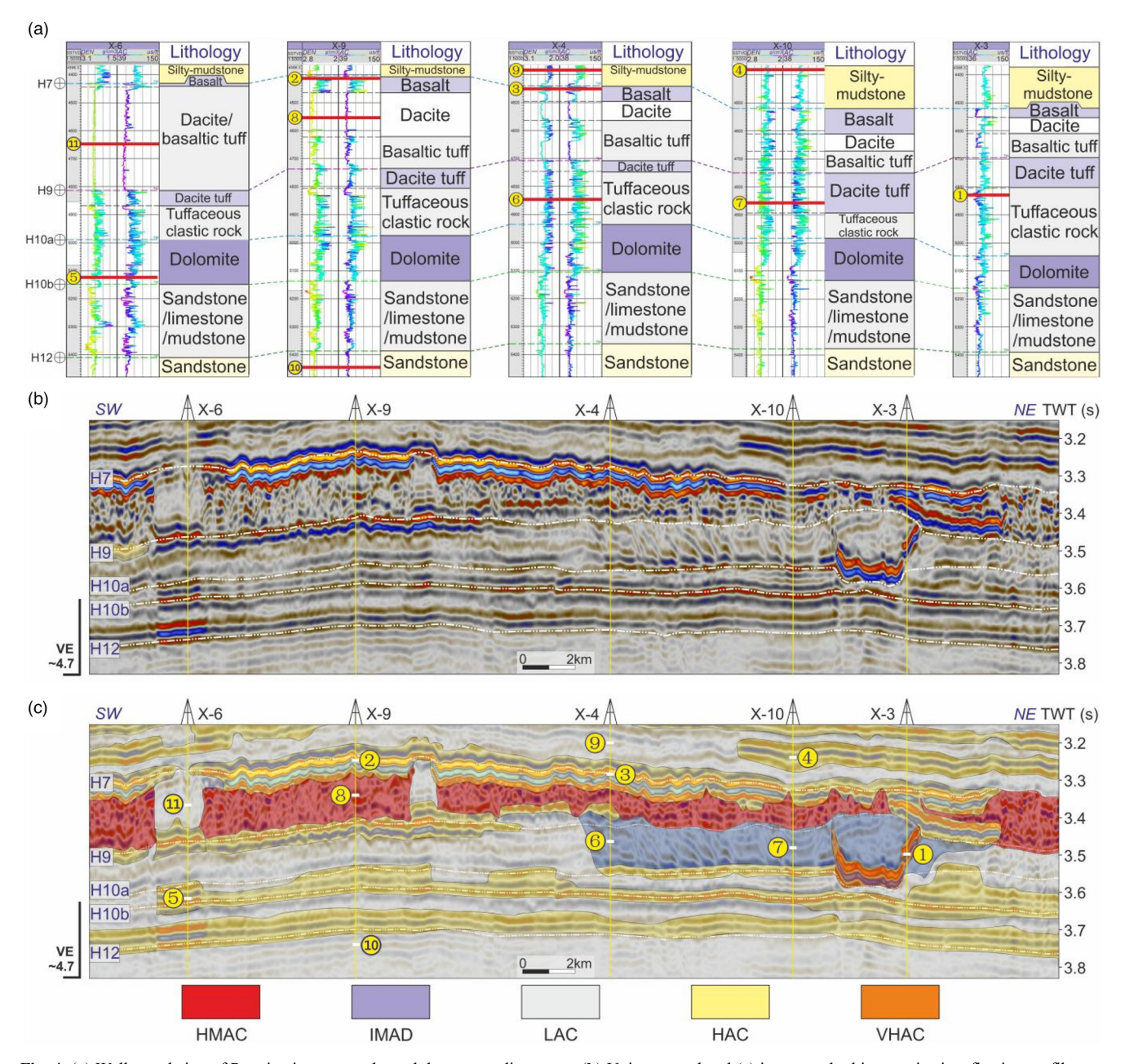


Fig. 4. (a) Well correlation of Permian igneous rocks and the surrounding strata. (b) Uninterpreted and (c) interpreted arbitrary seismic reflection profiles across the selected wells in (a). The wells and arbitrary seismic line are shown in Figure 3a. Numbers 1–10 indicate the seismic reflection facies (Table 1; Fig. 4c) and related well-log responses (Fig. 4a): ①, Very High Amplitude Continuous (VHAC); ②, ③, ④ and ⑤, High Amplitude Continuous (HAC); ⑤ and ⑦, Inclined Moderate Amplitude Discontinuous (IMAD); ⑥, High–Moderate Amplitude Chaotic (HMAC); ⑤, ⑥ and ⑥, Low Amplitude Continuous (LAC). VE, vertical exaggeration.

underlying and overlying reflectors. These erratic distribution patterns of seismic reflectors are likely to indicate a profound restructuring of the original strata. The restructuring potentially resulted from either substantial mass movement over a short period or *in situ* tectonic compression. The apparent absence of tectonically related faults or folds within the HMAC seismic facies (Fig. 4) favours the former interpretation.

The mass movement of significant sediment volumes, commonly resulting in mass transport complexes, often occurs during catastrophic events along basin margins, precipitated by slope failures (e.g. Ward et al. 2018; Wu et al. 2021). Similar features to those documented in mass transport complexes in seismic reflection data can be observed within the HMAC seismic facies, such as the chaotic or disrupted seismic reflections resulting from the disorganization of stratal layers (Wu et al. 2021), patches exhibiting high-amplitude reflections due to the presence of a relatively dense and consolidated mass (Nwoko et al. 2020), and some weak seismic reflection zones of

the disrupted and unconsolidated mass (Moscardelli *et al.* 2006). In addition, the variable thickness implies a transportation process, as no major erosional events are documented during middle–late Permian times in the study area (Xiao *et al.* 2020). Overall, the discontinuous, disrupted and hummocky geometry of the HMAC reflectors, occurring within a distinct stratigraphic unit, is consistent with the interpretation of a mass transport complex (cf. Moscardelli *et al.* 2006; Ward *et al.* 2018).

The DEN and AC wireline-log characteristics and published core interpretations (Xiao *et al.* 2020) of seismic facies HMAC indicate that it is composed of basalt, dacite and basaltic tuff (Fig. 4a). Northeastward thinning of the unit containing the HMAC seismic facies (Fig. 5a) indicates that the mass transport complex flowed in this direction, implying a SW to NE slope during deposition. The mass transport complex has a volume of 250 km³ in the study area, and thus requires mobilization and transport of a huge amount of volcanic and volcaniclastic material: for example, as a result of the

Table 1. Seismic facies scheme: High-Moderate Amplitude Chaotic (HMAC), Inclined Moderate Amplitude Discontinuous (IMAD), Low Amplitude Continuous (LAC), High Amplitude Continuous (HAC) and Very High Amplitude Continuous (VHAC) facies

Seismic facies	Seismic reflection	Geometry	Top reflections	Internal reflections	Base reflections	Reference colour
НМАС	0 1km	None	Very high amplitude, horizontal to sub- horizontal, parallel to sub-parallel reflections, undulating or occasionally discontinuous	Disrupted or hummocky, moderate to high reflection, randomly distributed reflections, difficult to identify	High amplitude, horizontal, parallel, continuous reflection	
IMAD	0 1km	Wedge	High to moderate amplitude, horizontal to sub-horizontal, parallel to sub-parallel reflections, with truncation	Moderate to high amplitude, consistently inclined, parallel to sub-parallel, discontinuous reflections	High to moderate amplitude, horizontal to sub-horizontal, parallel to sub-parallel termination or truncation	
LAC	0 1km	Sheet-like	Moderate to weak amplitude, horizontal to sub-horizontal reflections, parallel to occasionally discontinuous	Weak to moderate amplitude, parallel to sub-parallel, continuous reflections with some disruption, surrounding by chaotic reflections	Very high amplitude, horizontal to sub- horizontal, parallel to sub-parallel reflections with undulations	
нас	01km	Sheet-like	High amplitude, horizontal to undulating, parallel to sub-parallel, continuous reflections	High to moderate amplitude, horizontal to undulating, parallel to sub-parallel, continuous reflections	High amplitude, horizontal to undulating, parallel to sub-parallel, continuous reflections	
VHAC	01km	Planar transgressive	Low amplitude, horizontal to undulating, parallel to sub-parallel, continuous reflections	Very high amplitude reflections, occurring as very thin layers with only one pair of positive and negative amplitude reflections, concordant or discordant with surrounding strata	Low amplitude, discontinuous reflections	

catastrophic collapse of a volcanic centre. The onlap of overlying reflectors onto this unit indicates that it had an irregular top.

Seismic facies 2: Inclined Moderate Amplitude Discontinuous (IMAD)

Description

A unit of inclined, parallel to sub-parallel seismic reflectors of moderate—high amplitude occurs between horizons H9 and H10a in the northeastern part of the dataset (Figs 4 and 5). The unit is c. 0.1 s TWT thick (Figs 4 and 5). These reflectors constitute the Inclined Moderate Amplitude Discontinuous (IMAD) seismic facies (Table 1). In plan view, the inclined reflectors are arcuate and parallel to each other (Fig. 5b). The unit of IMAD seismic facies is locally overlain by the HMAC seismic facies, and its reflectors downlap the underlying HAC seismic facies. The IMAD unit passes laterally, to the SW, into the LAC seismic facies, with some individual reflectors being contiguous between the IMAD and LAC seismic facies (Figs 4b, c and 5c, d). The dip of the inclined reflectors is c. 5° relative to the near-horizontal reflectors above and below, assuming an average velocity of 4 km s⁻¹ (calculated from well X-10 at a depth of c. 4700 m: Fig. 4).

Calibration to wireline-log data

Wells X-4, X-10 and X-3 penetrate the IMAD seismic facies. The seismic facies exhibits AC values of $55-80 \,\mu\text{s/ft}$ for both wells X-4

and X-10 from 4750 to 4950 m, and well X-3 from 4700–4820 and 4860–5050 m (e.g. Fig. 4a, c), whereas DEN values of 2.3–2.5 g cm $^{-3}$ for wells X-4 and X-10 are present from 4750–4950 m.

Interpretation

The inclined reflectors in the IMAD seismic facies, relative to the near-horizontal reflectors above and below, indicate either layer-bound tectonic tilting or deposition on a palaeoslope. The former interpretation implies tilting and repetition of strata across a series of northward-dipping thrust faults: for example, at the toe of a second major mass transport complex that moved from north to south (cf. Moscardelli *et al.* 2006). Based on the high lateral continuity and sub-parallel, arcuate planform geometry of the inclined surfaces (Fig. 5b), and their contiguous relationship with sub-horizontal reflections in the LAC seismic facies to the SW (Figs 4b, c and 5c, d), we favour the latter interpretation of deposition on a palaeoslope as clinoforms. The set of inclined seismic reflections therefore delineates a prograding clinoform geometry.

Progradational clinoform-bearing successions often display downlap patterns, characterized by overlapping reflections onto older reflections, and toplap patterns, overlapped by younger reflections (e.g. Clairmont *et al.* 2021). Downlap is notably evident on horizon H10a above the HAC seismic facies (Fig. 5c–f), and the IMAD seismic facies also demonstrates toplap relationships with younger HMAC and HAC seismic facies along horizon H9 (Fig. 5c–f). The IMAD seismic facies is identified as comprising dacite tuff

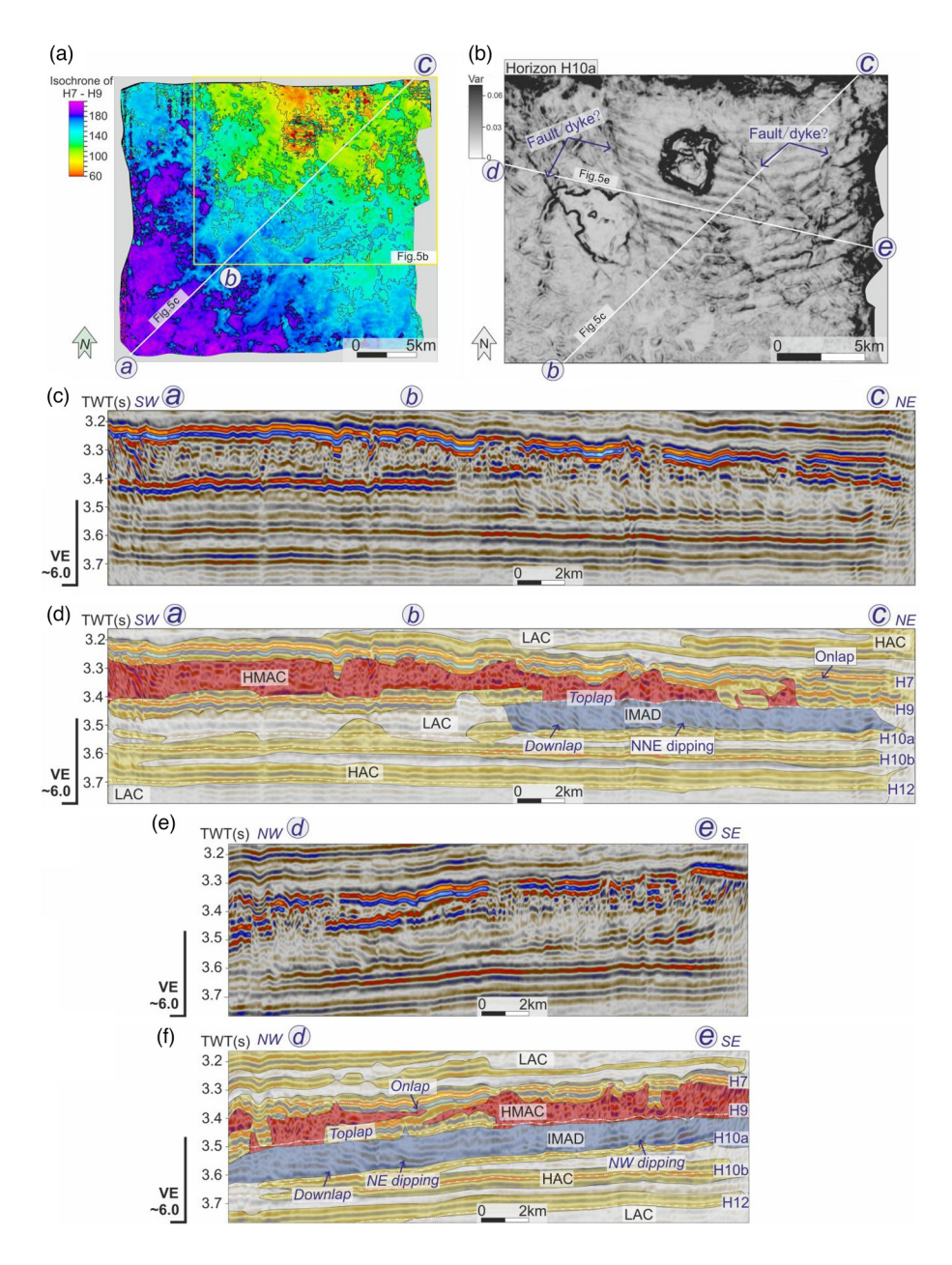


Fig. 5. (a) Time-thickness map between horizons H7 and H9. (b) Enlarged variance attribute map of horizon H10a; shown in (a). (c) and (e) Uninterpreted and (d) and (f) interpreted seismic reflection profiles across the study area; shown in (a) and (b). The profiles are orientated from SW to NE (c and d), and from SE to NW (e and f). Horizons H7, H9 and H10a are shown in Figures 2, 3b and 4b, c, and the seismic facies are summarized in Table 1. Interpreted seismic lines in (d) and (f) use the same key as in Figure 4c. VE, vertical exaggeration.

and tuffaceous clastic rocks, by comparison with the regional well-log responses of Xiao *et al.* (2020) and generic well-log responses of Rider and Kennedy (2011). These sedimentary deposits, primarily composed of volcanic material such as ash and debris, accumulated on inclined surfaces to form volcaniclastic clinoforms. Comparable examples have been well documented in the northern Faroe–Shetland Basin (Wright *et al.* 2012; Walker *et al.* 2022). Therefore, by implication, the IMAD seismic facies in the study area records progradational deposition of volcaniclastic clinoforms.

Seismic facies 3: Low Amplitude Continuous (LAC)

Description

The Low Amplitude Continuous (LAC) seismic facies consists of parallel to sub-parallel, continuous reflectors of weak to moderate amplitude (Table 1) (cf. the 'SPMAC seismic facies' of Dong *et al.* 2024). Intervals of LAC seismic facies are interspersed with intervals of HAC seismic facies above the H7 horizon and below the H10b horizon (Figs 4 and 5). The LAC seismic facies also occur in distinct regions enclosed by the HMAC seismic facies in the units between horizons H7 and H9 (Fig. 6c–j), and between horizons H9 and H10a lateral to the unit of IMAD seismic facies (Figs 4b, c and 5c, d).

Calibration to wireline-log data

Variable log-response values characterize the LAC seismic facies. First, DEN and AC values of 2.1-2.5 g cm⁻³ and 70-100 μs/ft, respectively, occur within the LAC facies above horizon H7 (e.g. 9 of X-4 in Fig. 4c) and between horizon H9-H10a (wells X-6, X-9 and X-10: Fig. 4). Second, a relatively uniform and narrow range of DEN and AC values of $2.40-2.50 \,\mathrm{g \, cm^{-3}}$ and $58-65 \,\mu\mathrm{s/ft}$, respectively, is present within these LAC reflectors between horizons H7 and H9 (e.g. @ of X-6 in Fig. 4c) and beneath horizon H12 (wells X-4, X-6, X-9 and X-10: e.g. @ of X-9 in Fig. 4c). Third, a wider range of DEN and AC values of 2.4- 2.8 g cm^{-3} and $60-85 \,\mu\text{s/ft}$, respectively, occurs between horizons H10b and H12 (wells X-3, X-4, X-6, X-9 and X-10: Fig. 4). These different well-log responses within the different parts of the studied strata indicate that different rock types occur in the LAC seismic facies, such that additional wireline-log or core data are required for further interpretation.

Interpretation

The sub-parallel to parallel reflections of the LAC seismic facies are consistent with the wireline-log responses of wells that penetrate

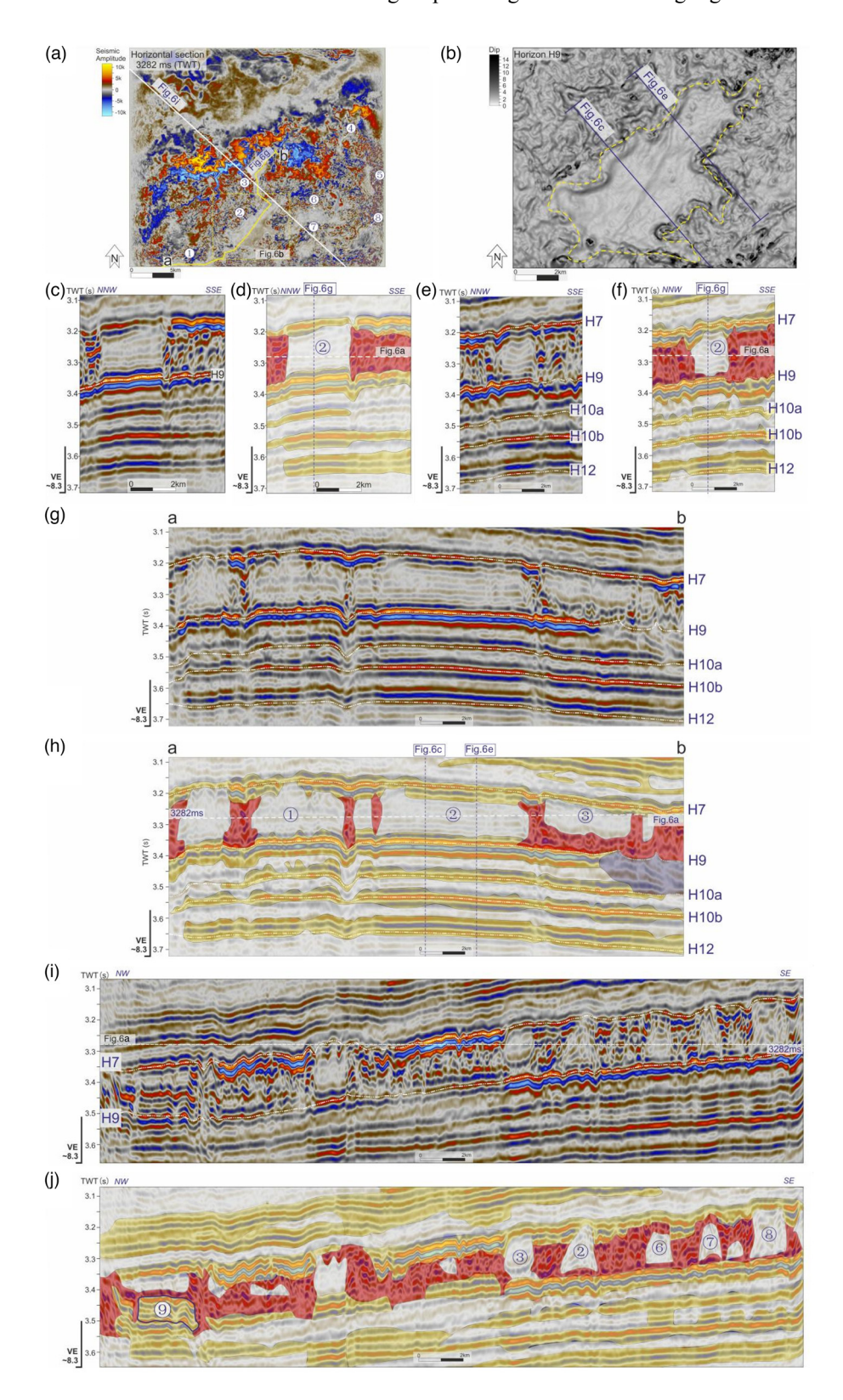


Fig. 6. (a) Time slice at 3.3 s TWT, showing eight discrete blocks (①—③) of the Low Amplitude Continuous (LAC) seismic facies (Table 1) encased in a unit of HMAC seismic facies (Fig. 4b, c). (b) Enlarged dip attribute map of horizon H9, highlighting one block of the LAC seismic facies (shown in Fig. 12a). (c), (e), (g), (i) Uninterpreted and (d), (f), (h), (j) interpreted seismic reflection profiles across blocks of the LAC seismic facies. ⑤ represents another HAC discrete block encased in the HMAC seismic facies (j). VE, vertical exaggeration.

them. Above horizon H7, the DEN and AC log responses indicate intercalated sandstones and mudstones, consistent with fluvial and deltaic deposits in the lower Triassic Ketuer Formation (Fig. 2) (Zhu et al. 2013; Deng et al. 2022). Between horizons H7 and H9, the DEN and AC log responses of the LAC seismic facies are similar to those of the HMAC seismic facies (e.g. Xiao et al. 2020), and are consistent with intercalated wackestone–packstone or dolomite, dacite and basaltic tuff (cf. Rider and Kennedy 2011). Core samples are not available to calibrate the lithology of the LAC seismic facies below horizon H10b (Xiao et al. 2020), but wireline-log responses indicate intercalated sandstones, wackestone–packstones and/or

mudstones (cf. Rider and Kennedy 2011), consistent with the regional stratigraphic context (Fig. 2).

Seismic facies 4: High Amplitude Continuous (HAC)

Description

The High Amplitude Continuous (HAC) seismic facies is characterized by continuous to undulating, horizontal to subhorizontal parallel reflectors of high-moderate amplitude (Table 1) (cf. the 'PVHAC seismic facies' of Dong *et al.* 2024). Intervals of

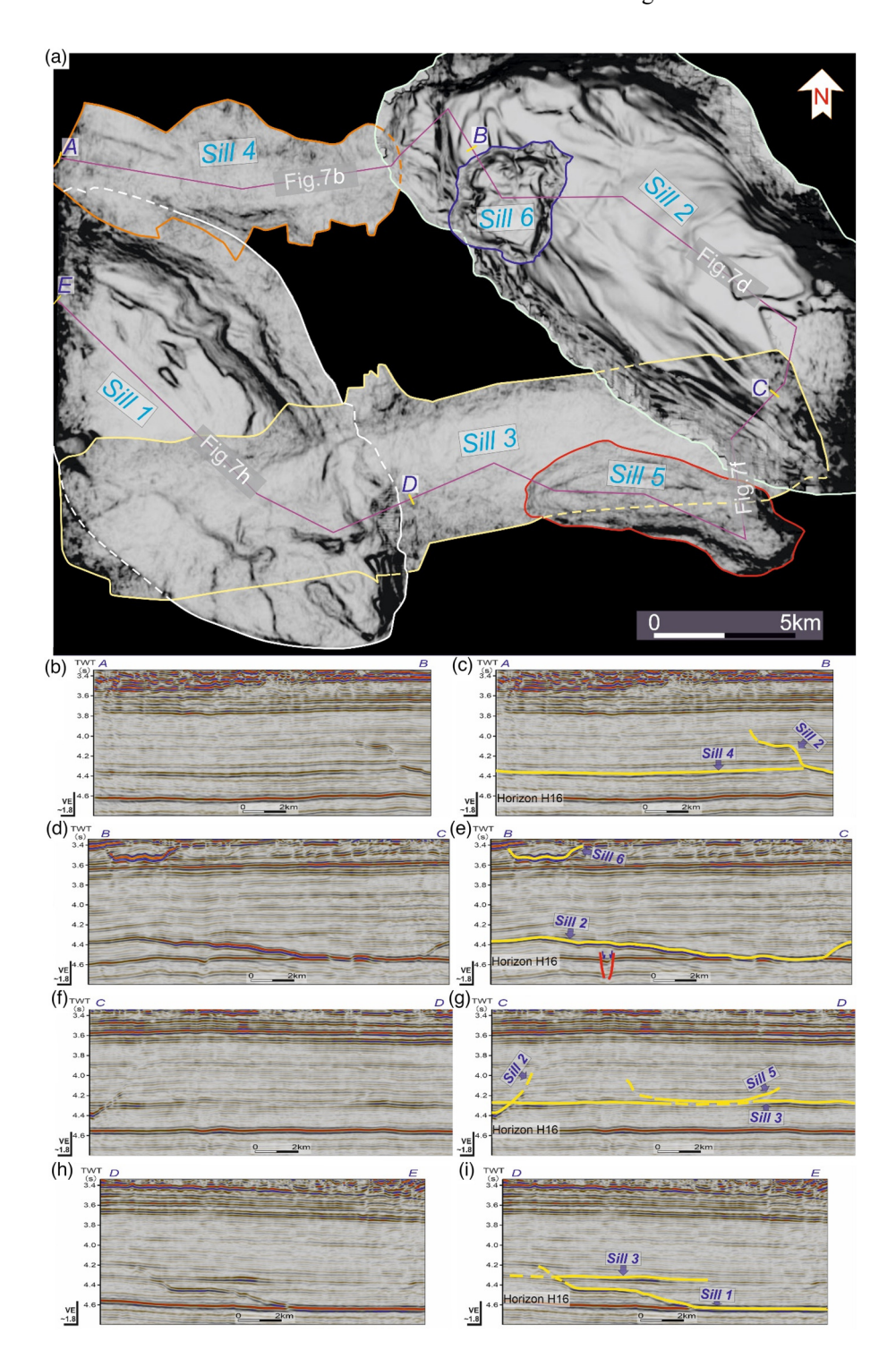


Fig. 7. (a) Plan view of intrusive sills developed at different depths within the seismic dataset, shaded by variance attribute and with the intervening rocks not visualized. A–E indicate the profile lines. (b), (d), (f), (h) Uninterpreted and (c), (e), (g), (i) interpreted seismic reflection profiles across sills; see (a) for the locations of the profiles. VE, vertical exaggeration.

the HAC seismic facies that are $\it c.~0.02$ s TWT (50–70 m) thick alternate with those of the LAC seismic facies above horizon H7 and below horizon H10a, and occur along horizon H9 where they are locally truncated by the HMAC seismic facies.

Calibration to wireline-log data

The HAC seismic facies corresponds to a range of well-log responses. DEN and AC values of 2.0–2.4 g cm $^{-3}$ and 75–100 $\mu s/$ ft, respectively, occur in the HAC seismic facies above horizon H7 (wells X-3, X-6 and X-10: Fig. 4). Similar DEN and AC values of 2.1–2.7 g cm $^{-3}$ and 70–100 $\mu s/$ ft, respectively, characterize the HAC seismic facies along horizon H7 (wells X-3, X-4, X-6, X-9 and X-10: e.g. @ of X-9 in Fig. 4) and along horizon H9 (wells X-3, X-6

and X-9: Fig. 4). In general, the HAC seismic facies along horizon H10b exhibits DEN and AC values of 2.3–2.7 g cm⁻³ and 60–100 μ s/ft, respectively (wells X-3, X-4, X-6, X-9 and X-10: e.g. ⑤ of X-6 in Fig. 4), and along horizon H12 exhibits DEN and AC values of 2.4–2.8 g cm⁻³ and 55–75 μ s/ft, respectively (wells X-3, X-4, X-6, X-9 and X-10: Fig. 4).

Interpretation

High-amplitude seismic reflections record an acoustic impedance contrast between adjacent rock layers, and could result from, for example, abrupt variations in rock type. Both sandstone and mudstone are preserved in lower–middle Triassic strata in the study area (Liu *et al.* 2012; Guo *et al.* 2015; Li *et al.* 2023). The variability

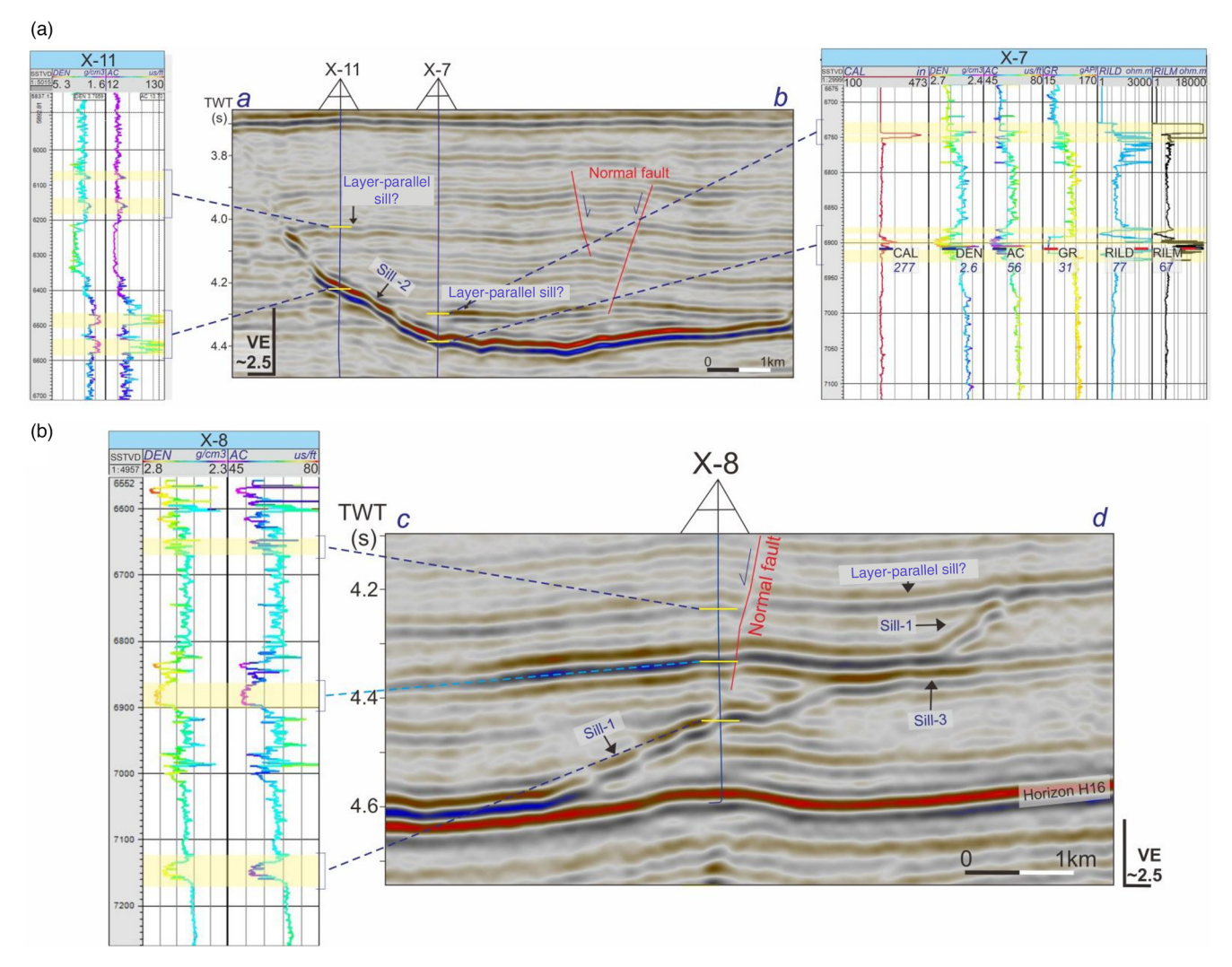


Fig. 8. (a) and (b) Examples of intrusive sills in seismic reflection profiles that are calibrated to well-log responses. The locations of the profiles are shown in Figure 3a. SSTVD, subsea true vertical depth; VE, vertical exaggeration.

in the sandstone content and the intercalation of mudstone within the sandstone in the Triassic strata above horizon H7 therefore result in the presence of the HAC seismic facies.

An interval of the HAC seismic facies around horizon H7 corresponds to a relatively high-density and fast P-sonic velocity log response, relative to the underlying and overlying intervals of the LAC seismic facies, and coincides with a prominent basalt layer (Fig. 4). Discrete regions of the HAC seismic facies developed within the unit of HMAC seismic facies potentially represent basalt blocks within the mass transport complex (Figs 5c–f and 6i, j). The interval of HAC seismic facies surrounding horizons H10a and H12 is interpreted as dolomite-rich strata (cf. Rider and Kennedy 2011).

Seismic facies 5: Very High Amplitude Continuous (VHAC)

Description

Very-high-amplitude but thin reflectors, usually present as a pair of negative and positive amplitudes (Fig. 4) that are either concordant or disconcordant with the surrounding reflectors, constitute the Very High Amplitude Continuous (VHAC) seismic facies (Table 1). For example, Figure 4b and c shows a body of VHAC seismic facies in the northeastern part of the study area that has a concave-upward geometry and irregular base that truncates the underlying horizon

H10a, is discordant with the overlying unit of IMAD seismic facies, and is associated with domal relief of the overlying horizon H9. Other bodies of VHAC seismic facies occur below horizon H12 and have a similar concave-upward, saucer-shaped geometry, with the amplitude of reflectors in the seismic facies gradually weakening at both steeply inclined margins of the bodies (e.g. Fig. 3b, c). Saucer-shaped bodies of the VHAC seismic facies also intersect planar bodies of the VHAC seismic facies (Fig. 4; see also Supplementary Fig. S1).

Calibration to wireline-log data

The VHAC seismic facies is penetrated at depths of 4830 m in well X-3 (① in Fig. 4a), 6760 and 6900 m in well X-7, 6530 and 6120 m in well X-11, and 6890 and 7150 m in well X-8 (Fig. 8). At these locations, the VHAC seismic facies has DEN and AC values of 2.5–2.7 g cm⁻³ and 40–53 μ s/ft, respectively.

Interpretation

The log responses of the VHAC seismic facies, characterized by significantly higher density and lower acoustic slowness than the surrounding sediments (e.g. sandstone, mudstone and wackestone–packstone), suggest a composition that is likely to be dominated by volcanic rocks. The irregular, discordant to concordant geometry and widespread distribution of bodies of the VHAC seismic facies

12 X. Dong et al.

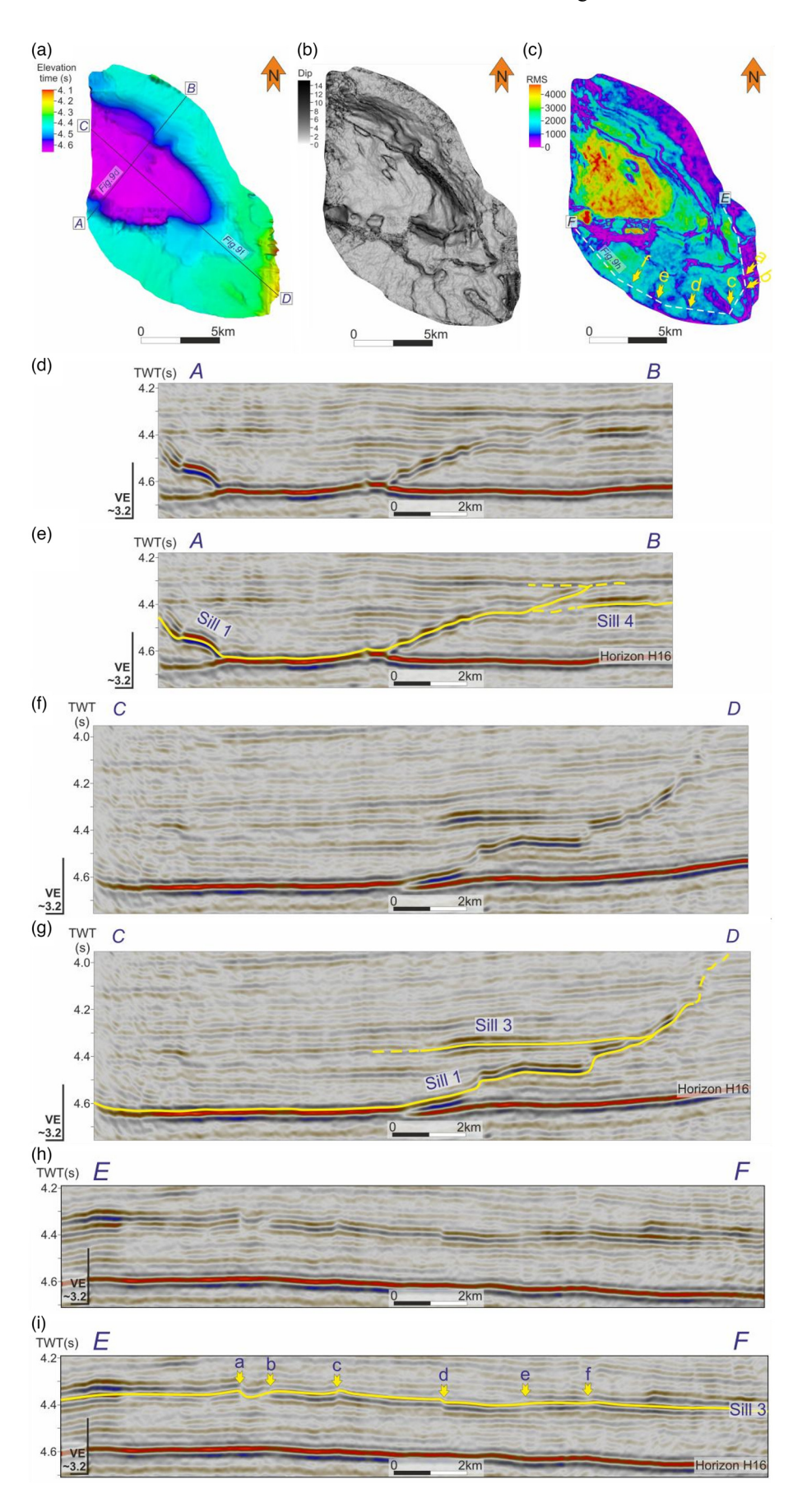


Fig. 9. (a) Time—structure map; (b) dip attribute map; and (c) RMS amplitude map of the top Sill 1 reflector; and (d), (f), (h) uninterpreted and (e), (g), (i) interpreted seismic profiles across Sill 1; see (a) and (c) for the profile locations. The profiles are orientated along the short axis (d and e), along the long axis (f and g) and around the southeastern margin of the sill (h and i). 'a'-'f' in (c) and (i) are 'step' features around the outer rim of Sill 1. VE, vertical exaggeration.

indicate that it represents intrusive igneous rocks, either gabbro or diabase (e.g. Ma *et al.* 2013, 2017). This interpretation is consistent with the large acoustic impedance contrast with the surrounding sedimentary strata implied by the high-amplitude character of

reflectors in the seismic facies. Cores from rocks of similar seismic character sampled diabase and gabbro in the nearby Tabei Uplift (Tian *et al.* 2010; Gao *et al.* 2017; Ji *et al.* 2020) and Tazhong Uplift (H. Li *et al.* 2017).

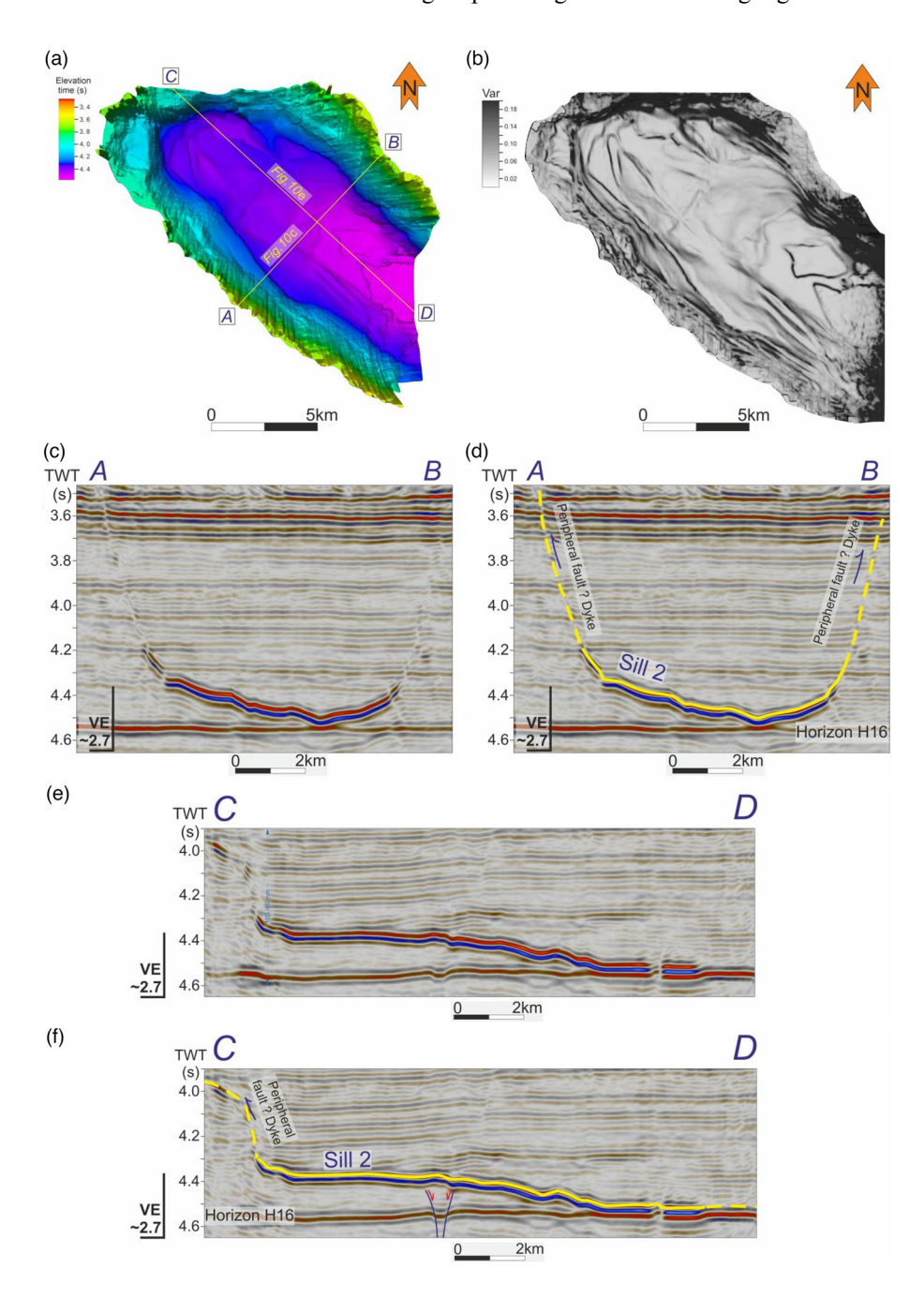


Fig. 10. (a) Time—structure map; (b) dip attribute map of the top Sill 2 reflector; and (c) and (e) uninterpreted and (d) and (f) interpreted seismic profiles across Sill 2 see (a) for the profile locations. Profiles are orientated along the short axis (c and d) and along the long axis of the sill (e and f). VE, vertical exaggeration.

Results: characterization of igneous and volcaniclastic rocks

Sill morphology and spatial configuration (VHAC seismic facies)

Description

Six sills marked by the VHAC seismic facies have been mapped within the dataset (Figs 7 and 8). The sills can be grouped into two distinct geometrical types: concordant, bedding-parallel sills; and discordant, saucer-shaped sills (Tables 2 and 3). Sills 1, 2, 5 and 6 are saucer-shaped, and exhibit a geometry consisting of three parts: a flat inner sill, inclined sheets and, commonly, flat outer sills (e.g. Fig. 9) (cf. Planke *et al.* 2005). Sills 1 and 2 extend outside of the study area. Sills 3 and 4 exhibit a bedding-parallel geometry. All sills occur in upper Ordovician–middle Permian strata, between horizons 16 and 9 (Figs 3, 4 and 7) at present-day depths of 3.4–4.6 s TWT. Sills 1–5 have areal extents of 25–115 km² and are oval to rectangular in plan view but vary in the direction of elongation

(Figs 7a, 9a–c and 10a, b; Table 3; see also Supplementary Figs S2A–C, S3A–C and S4A, B). Some saucer-shaped sills exhibit a stepped morphology in their long-axis orientation (e.g. Figs 9d–g and 10e, f), with steps corresponding to high-RMS-amplitude lobes that extend outwards towards the sill margin (e.g. Fig. 9c, f–i). They exhibit a radially extending, irregular appearance, with en echelon steps trending in various directions (e.g. step offsets 'a' to 'f' in Fig. 9c, i), while the offset increases progressively along the flow direction (e.g. step offset 'e' in Fig. 9c). In contrast, Sill 6 is 10 km² in area and approximately circular in plan view (Fig. 11; Table 3; see also Supplementary Fig. S1). Horizon H9 is folded above saucershaped Sill 6, defining an anticlinal dome that is onlapped by overlying strata (Fig. 11; see Supplementary Fig. S1).

Sills 1–5 intersect each other (Fig. 7b–i), whereas Sill 6 is isolated (Fig. 7d, e). Sill 1 intersects Sill 3 along its southwestern and southeastern margins, and Sill 4 along its northern margin. Sill 2 intersects Sill 4 and Sill 3 along its northwestern and southwestern margins, respectively. Sill 3 intersects Sill 5 along its southern margin. Sill intersections have three types of geometrical

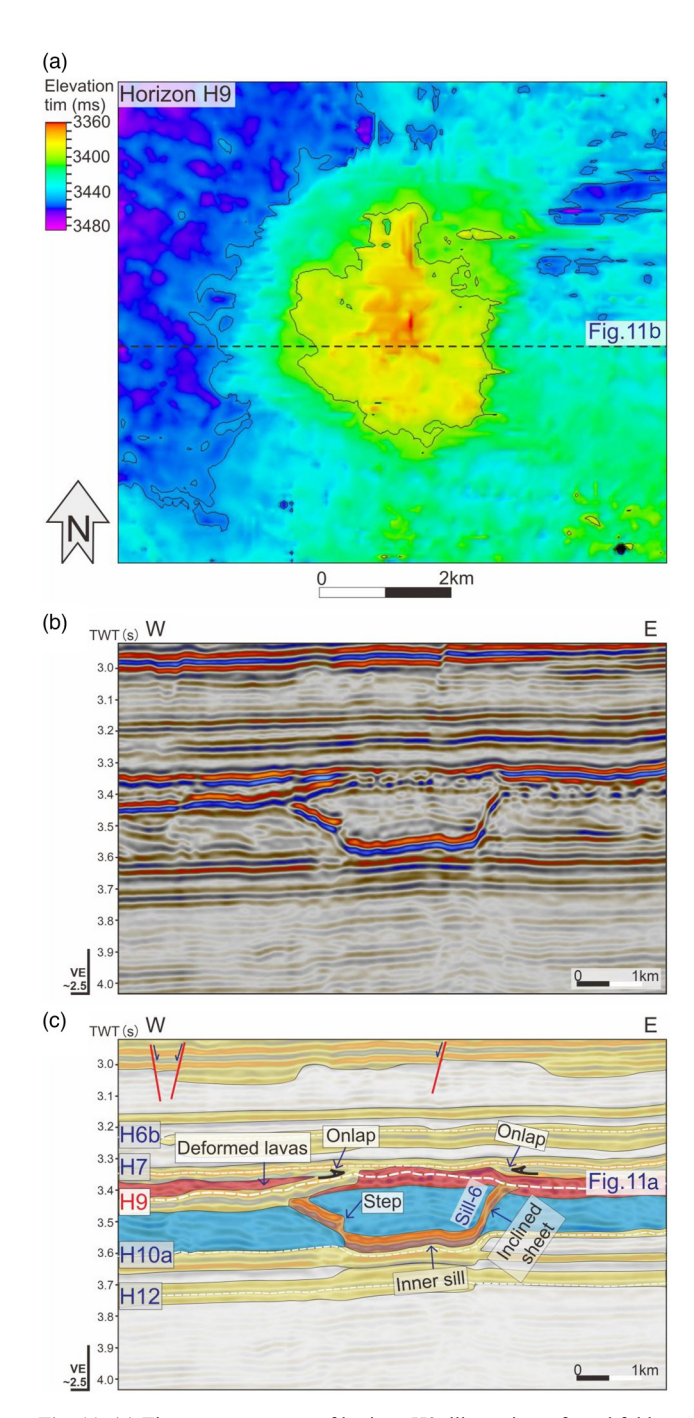


Fig. 11. (a) Time—structure map of horizon H9, illustrating a forced fold above Sill 6 (see Supplementary Fig. S1); and (b) uninterpreted and (c) interpreted seismic profile across the fold. Horizon H9 is shown in Figures 2, 3c and 4b, c; and the seismic facies are summarized in Table 1. VE, vertical exaggeration.

configuration (cf. Hansen *et al.* 2004): (1) a 'T-type' intersection in which the steeply inclined margin of a deeper sill terminates against the flat central portion of a shallower sill (Fig. 12g, h; see also Supplementary Fig. S2D, E) or the flat margin of a deeper sill terminates against the steeply inclined margin of a shallower sill (see Supplementary Fig. S3F, G); (2) an 'X-type' in which both sills extend beyond their intersection (Fig. 12b, c; see also Supplementary Fig. S2D, E); and (3) a 'U-type' intersection in which a shallower, saucer-shaped sill rests above a deeper, bedding-parallel sill (Fig. 12d, e; see also Supplementary Fig. S4C–F). In addition, Sill 3 cuts across a strike-slip fault (see Supplementary Fig. S2D–G).

Interpretation

Bedding-parallel sills, such as sills 3 and 4 (Fig. 7a; see also Supplementary Figs S2 and S3), form along weak stratal interfaces (e.g. Planke et al. 2005). Sills 3 and 4 have both developed along horizon H15, which is the interface between the muddy limestones of the late Ordovician Sangtamu Formation and the sandstones of the early Silurian Kepingtage Formation (Fig. 2a). The lithological contrast between these formations is likely to have contributed to the presence of a weak stratal interface here, resulting in the development of planar sills at their interface. Saucer-shaped sills, such as sills 1, 2, 5 and 6 (Figs 7a and 9–11; see also Supplementary Figs S1 and S4), can develop from bedding-parallel sills because the initial doming of the overburden, as the sill spreads parallel to a surface layer, causes asymmetrical stresses to accumulate and then trigger inclined sheet initiation when the sill reaches a critical diameter (e.g. Malthe-Sørenssen et al. 2004; Galland et al. 2009; Yao et al. 2018). The areally extensive, bedding-parallel centres of sills 1 and 2 are developed along horizon H16 (Figs 9 and 10), marked by an unconformity between wackestone-packstonegrainstones of the middle Ordovician Yijianfang Formation and the overlying mudstone-wackestone of the late Ordovician Oiaerbake Formation (Fig. 2). Feeder dykes below sills 1 and 2 are not apparent in the study area, implying that they are either absent or not imaged, because they are steeply dipping. Subvertical dykes feeding the overlying sills have been penetrated by a cored well at a depth of 6 km in Ordovician carbonate strata in the nearby Tabei Uplift (Gao et al. 2017).

Divergence in the orientation of high-RMS-amplitude lobes on the flat outer rim of saucer-shaped sills (e.g. Fig. 9c) is attributed to preferential magma propagation along different horizons (Goulty and Schofield 2008). This phenomenon gives rise to the development of distinct 'steps' in the sill geometry that are orientated parallel to the magma flow and sill propagation direction (Francis 1982; Rickwood 1990; Schofield *et al.* 2012*a*, *b*; Magee *et al.* 2018).

The mechanical stresses associated with rising overpressured fluid (magma) in an area where the minimum stress corresponds to the vertical confining pressure cause magma to preferentially flow laterally along bedding planes. Magma subsequently moves upwards when encountering a zone of weakness, such as a fault surface, via a dyke (Schofield et al. 2012a; Walker 2016). Thus, inclined sheet-like sections of the seismically imaged sills, which extend c. 3 km laterally and c. 500 m vertically within layered sediments (e.g. Sill 6: Fig. 11; Table 3), may in fact comprise small (subseismic), layer-parallel sills connected by vertical dykes, resulting in a characteristic 'stair-step' morphology (e.g. Johnson and Pollard 1973; Polteau et al. 2008). For example, observations of geometrically analogous, seismically imaged sandstone intrusions in cores reveal that small-scale sills (c. 30 cm thick) tend to connect thicker dykes and sills (Lonergan et al. 2007). Numerical modelling of sill growth suggests that the asymmetry of the stress field, caused by the uplift of the overburden, results in the sill tip bending upwards. However, its ascent is constrained by a reduction in pressure inside the sill due to extension above its neutral buoyancy level (Malthe-Sørenssen et al. 2004). A similar process may explain the development of sills in the study area, although the details remain unclear due to the limitations of the seismic resolution.

The high-RMS-amplitude lobes in Sill 1 mark 'steps' developed along its southeastern margin (Fig. 9c, h, i), which indicates a SE-outward expansion of magma flow. Westward weakening of the RMS amplitude corresponds to westward thinning of the sill (see Supplementary Fig. S2B), and may indicate that Sill 3 was fed by magma intruded from Sill 2 and propagated westwards along a weak stratal interface. A similar west to east RMS weakening trend

Table 2. Types of sill geometry (modified after Planke et al. 2005; Galland et al. 2009)

Sill facies unit	Seismic reflection	Description
Layer parallel		The sill develops conformably along the strata, displaying high-amplitude, smooth seismic reflections and strong continuity
Saucer-shaped		The sill intersects with the strata, displaying high-amplitude, irregular seismic reflections and a tendency to thicken toward the centre of the saucer

in Sill 4 may indicate magma flows towards the east, but the potential magma feeder is not identified (see Supplementary Fig. S3B).

The anticlinal dome in strata above saucer-shaped Sill 6 (e.g. horizon H9 in Fig. 11; see also Supplementary Fig. S1) is interpreted as a 'forced fold' caused by uplift above ascending magma at shallow depths (cf. Magee *et al.* 2017; Tian *et al.* 2021). Onlap of horizon H7 and the underlying strata onto domed horizon H9 (Fig. 11) therefore implies that Sill 6 was intruded during the lower—middle Permian (Fig. 2).

Volcaniclastic shoreline and clinoform set (IMAD seismic facies)

Description

The IMAD seismic facies in the northeastern part of the dataset defines a set of clinoforms c. 0.1 s TWT high with an arcuate planview geometry (Figs 4 and 5). They have an estimated dip angle of about 5°. Wells penetrating the IMAD seismic facies indicate that the clinoform set is composed of dacite tuff and tuffaceous clastic sedimentary rocks (Fig. 4).

Interpretation

Clinoforms in the IMAD seismic facies indicate deposition on a dipping stratigraphic surface, while the arcuate plan-view geometry of the clinoforms resembles a strandplain developed between two wave-dominated deltaic headlands (cf. Jackson et al. 2010; Cross et al. 2015; Zimmer et al. 2019; Berton et al. 2021). Similar features are reported in seismic reflection data from volcanic strata in the Faroe-Shetland Escarpment, offshore UK (Planke et al. 1999; Wright et al. 2012), the More Marginal High (Walker et al. 2022) and the Vøring Escarpment, offshore Norway (Berndt et al. 2012; Abdelmalak et al. 2016; Planke et al. 2017), the West Indian Continental Margin in the northern Arabian Sea (Corfield et al. 2010), and the Bay of Bengal (Ismaiel et al. 2017), where they are interpreted as volcaniclastic and lava-fed shorelines. Outcrop analogues include hyaloclastite breccia clinoforms in West Greenland (Pedersen et al. 1998) and Iceland (Greenfield et al. 2020), and lava-fed shorelines in Hawaii (Di Traglia et al. 2018) and Antarctica (Smellie et al. 2013). Volcaniclastic shorelines and lavafed shorelines exhibit similar geometrical features to siliciclastic shorelines, but may record much greater variations in the volcanogenic sediment supply, especially during flood-basalt eruptions (Wright et al. 2012). Lava-fed shorelines are characterized by large, steeply dipping subaqueous hyaloclastite breccia foresets and subhorizontal, subaerial lava-flow topsets (Wright et al. 2012; Smellie et al. 2013; Maharjan et al. 2024). Lava-fed deltas are steep, with dip angles of up to c. 20° (e.g. Wright $et\ al.\ 2012$; Maharjan et al. 2024). Volcaniclastic clinoform deposits along depositional strike of such deltas, fed by sediment reworking and transport, display gentler dip angles of less than 10° (e.g. Clairmont et al. 2021). The latter are similar to the clinoforms identified in this study.

Polygonal ridges and depressions at the base of the mass transport complex (HMAC seismic facies)

Description

Polygonal ridges and intervening depressions are developed in the HAC seismic facies around horizon H9, directly below the HMAC seismic facies (Figs 5, 6 and 13c, d). These ridges and depressions have an amplitude of 0.01–0.02 s TWT (c. 20–40 m: Fig. 13d), and are imaged mainly in the southwestern part of the study area (Fig. 13a–c). They have a lateral spacing of 800–1000 m. Parts of the ridges also extend upwards into the HMAC seismic facies, and corresponding depressions extend downwards into the HAC seismic facies (Fig. 13d).

Interpretation

The ridges and depressions are not associated with erosional relief, which discounts their interpretation as palaeovalleys filled with basalt (cf. Bromley et al. 1970; Watt and Watt 1971; Olierook et al. 2015), channelized lava flows and/or lava tubes (e.g. Sauro et al. 2020; Kim et al. 2022; Tomasi et al. 2022). Instead, we interpret the ridges as polygonal flame structures, diapiric walls and/or faults resulting from the loading of poorly compacted tuffs and tuffaceous sediment (HAC seismic facies) by a large-volume, rapidly emplaced mass transport complex (HMAC seismic facies) and associated dewatering (e.g. Berndt et al. 2012). The polygonal geometry of the ridges and depressions implies that horizontal stress during dewatering was isotropic. Similarly sized polygonal features in volcanic strata have been reported at the top of the Austin Chalk Formation in the Maverick Basin, South Texas, USA (Ogiesoba et al. 2015), and at the base of Paleogene basalt layer in the Vøring Margin, offshore mid-Norway ('egg-box network': Maharjan et al. 2024).

Dacite megaclasts (LAC seismic facies) and basalt megaclasts (HAC seismic facies) within the mass transport complex (HMAC seismic facies)

Description

The unit of HMAC seismic facies between horizons H9 and H7, interpreted above as a mass transport complex composed of dacite and basaltic tuff, contains discrete, sharp-sided regions of LAC and

Fable 3. Sill measures and position information: the velocity model used for the depth conversion is taken from Sun et al. (2021)

		Area Major (km²)	Major axis (km)	Minor axis (km)	Major axis Minor axis Aspect ratio Maxii (km) (major axis/ minor axis) (km)	Maximum depth (km)	Height (km)	Maximum depth Height Position relative to extrusive layers Top sill termination depth (km)	Top sill termination depth
Disco	Discordant, saucer-shaped	c. 70	13	10	1.30	c. 7.4	c. 1.5 Below	Below	Above the Kepingtage Formation
Disco	Discordant, saucer-shaped	c.50	12	&	1.50	c. 7.2	c. 1.3	Below	Above the Tataaiertage Formation
Concc	Concordant, bedding-parallel c. 115	c. 115	22	5	4.40	c. 6.9	c. 0.3	Below	Above the Sangtamu Formation
Concc	Concordant, bedding-parallel	c. 45	10	4	2.50	c. 6.9	c. 0.1	Below	Above the Lianglitage Formation (probably)
Disco	Discordant, saucer-shaped	c.26	6	3	3.00	c. 6.6	c. 0.6	Below	Above the Tataaiertage Formation
Disco	Discordant, saucer-shaped	c. 10	3	3	1.00	c. 5.0	c. 0.5	Within	Below the Nanmin Formation

HAC seismic facies (Figs 4 and 6). These regions of LAC and HAC seismic facies exhibit continuous parallel—sub-parallel reflectors internally (Fig. 6c–j). At least eight distinct regions of the LAC seismic facies occur in the southeastern part of the study area (Fig. 6a). These regions are large (4–10 km² in plan view: Fig. 6a; and are up to 170 ms TWT, or c. 400 m, thick: Fig. 6c–j) have irregular, sharp-sided shapes (e.g. Fig. 6b), exhibit a disorganized plan-view distribution (Fig. 6a), and lie along or above the basal surface of the mass transport complex (Fig. 6c–j). Velocity pushdown is evident at the margins of the regions of the LAC seismic facies (Fig. 6c, e, g), caused by high velocities within the LAC regions relative to the surrounding HMAC seismic facies.

Interpretation

Well X-6 penetrates a sharp-sided region of the LAC seismic facies (① in Fig. 4). DEN and AC logs in the LAC region exhibit uniform responses that are similar in value to the dacite strata penetrated by well X-9 (③ in Fig. 4) (cf. core sample from well X5-5H in fig. 4 of Xiao et al. 2020). In the context of the large mass transport complex represented by the HMAC seismic facies, the regions of the LAC seismic facies are therefore interpreted as dacite megaclasts. Sharp-sided regions of the HAC seismic facies (⑨ in Fig. 6j) are interpreted as basalt megaclasts, based on their seismic facies character and association with basaltic tuffs within the HMAC seismic facies unit. These megaclasts are blocks of relatively undeformed strata carried by mass flow due to its high cohesive strength (cf. Hodgson et al. 2018; Nwoko et al. 2020; Wu et al. 2021). Similar volcanic megaclasts have been reported in recent lava flows and pyroclastic flows (Guest and Sánchez 1969; Sato et al. 1992)

Channels and fans at the top of the mass transport complex (HMAC seismic facies)

Description

The top of the mass transport complex represented by the HMAC seismic facies lies below horizon H7, and displays pronounced relief (Figs 4, 5c–f and 6c–j). This relief is associated with depressions that are c. 0.1 s TWT deep ('d' in Fig. 13d) and some depressions can be traced on horizon chaos maps or with high-RMS amplitudes as sinuous or irregular channels that are several kilometres to tens of kilometres in length (Fig. 13a, b). Moreover, distinctive 'fan-like' geometrical features have developed on the top of the mass transport complex (Fig. 14a, i, j). These features encompass an area of c. $7 \, \mathrm{km}^2$ individually, with irregular branching structures emanating from the 'fan axis' and extending towards the periphery of the fan structure. The 'fan axis' is linked to an area characterized by high seismic amplitude and vertically uplifted geometry (Fig. 15).

Interpretation

We have interpreted the channelized depressions as fluvial channel belts formed at horizon H7, consistent with the continental palaeoenvironment of upper Permian strata (Li *et al.* 2011; Lin *et al.* 2012). The presence of high-RMS amplitudes within some channelized depressions may suggest lava filling the channels, analogous to examples reported in the South China Sea (Sun *et al.* 2019). Alternatively, these depressions could represent remnants of a polygonal network, akin to similar depressions observed in the NW part of the dataset (Fig. 13a). The discontinuous extent and distribution of these depressions may be attributed to later tectonic activity, sedimentary processes involving erosion, or alteration.

The 'fan-like' geometrical features are interpreted as lava-fed fans atop the mass transport complex. Typically, a lava-fed fan

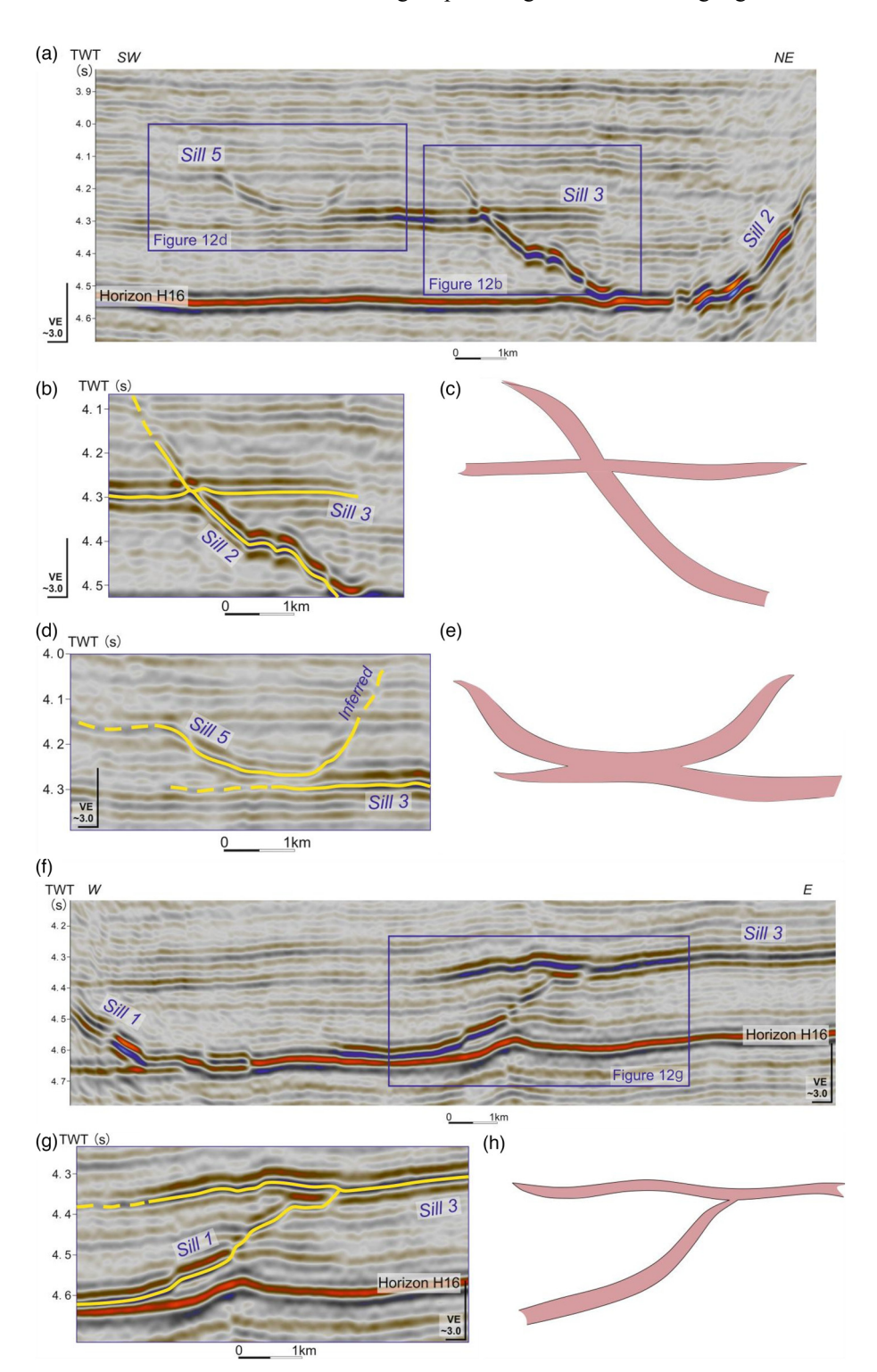


Fig. 12. (a) Uninterpreted seismic reflection profile across sills 2, 3 and 5; (b) and (d) interpreted details of the seismic reflection profile (a) showing the geometrical relationships between sills 2 and 3, and between sills 3 and 5, respectively; and (c) and (e) schematic representations of these geometrical relationships (b) and (d). (f) Uninterpreted seismic reflection profile across sills 1 and 3; (g) interpreted detail of the seismic reflection profile showing the geometrical relationship between sills 1 and 3; and (h) schematic representations of these geometrical relationships (g). VE, vertical exaggeration.

comprises lava-flow channels, a lava-flow apron and volcanic edifices serving as the magma source (Sun et al. 2019). No distinct volcanic edifices have been identified in the study area. However, these lava-fan structures are linked with deep, vertical, high-amplitude features that may indicate the feeding path or magma-migration path, similar to vertical magma-migration paths observed in the Vøring and Møre basins (Planke et al. 2005).

Relationship between extrusive and intrusive rocks

Description

Several sills (VMAC seismic facies) are associated with subvertical zones of disrupted and/or low reflectivity that extend upwards from the highly reflective sill margins and define short (2000–10 000 m)

curvilinear features in plan view (Figs 14 and 15). Some subvertical zones of disrupted reflectivity are associated with the cut-off and displacement of strata, and they bifurcate upwards (Fig. 15). Stratal reflections between the upward-bifurcating zones of disrupted reflectivity can exhibit anticlinal folding and high reflectivity (Fig. 15c-f). Sill 1 appears to be displaced by the strike-slip fault documented in the study area, while Sill 2 cuts across the same strike-slip fault and related en echelon normal faults that develop above it (Fig. 16).

Interpretation

Subvertical zones of weak seismic reflectivity are characteristic of connection paths between intrusive sills and extrusive volcanic

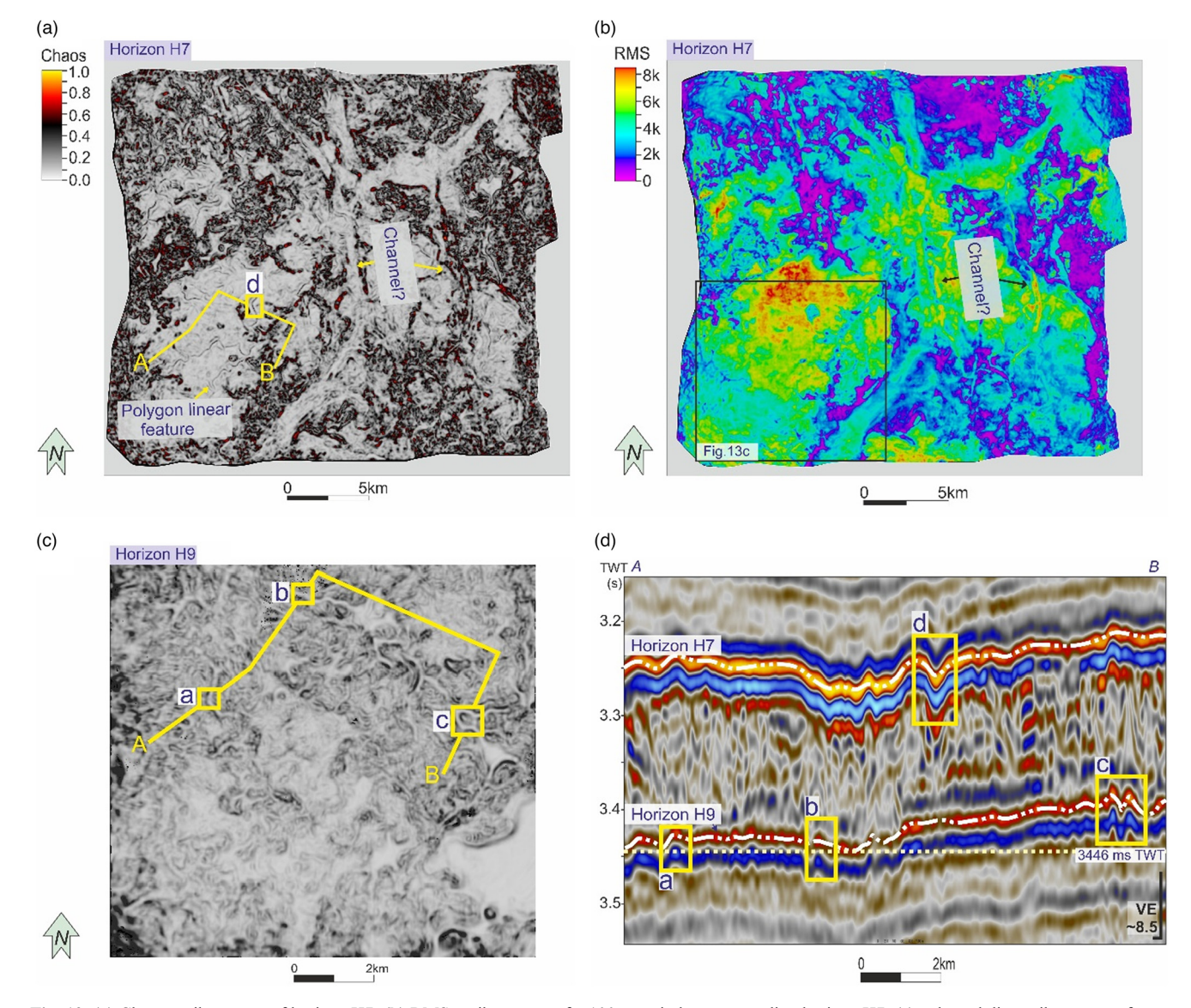


Fig. 13. (a) Chaos attribute map of horizon H7; (b) RMS attribute map of a 100 ms window surrounding horizon H7; (c) enlarged dip attribute map of horizon H9, located in (d); and (d) arbitrary seismic reflection profile through the interval containing horizons H7 and H9, showing polygonal ridges and intervening depressions on horizon H9, and linear depressions on horizon H7. Horizons H7, H9 and H10a are shown in Figures 2, 3c and 4b, c. VE, vertical exaggeration.

rocks in sedimentary basins (Thomson 2007). Such weak reflectivity zones are interpreted as near-vertical faults that connect the tips of a sill to uplifted 'eye-shaped', 'mound-shaped' and 'crater-shaped' strata (Planke *et al.* 2005), including in the Tarim Basin (Yao *et al.* 2018; Ji *et al.* 2020; Liu *et al.* 2022). We similarly interpreted the subvertical zones in the study area as the connection between intrusive sills and extrusive rocks, marked in two cases by lava-fed fans at horizon H7 (Figs 14 and 15).

Dykes and sills can play a significant role in the transport of magma and the feeding of overlying eruptive complexes in shallow-level volcanic systems (Pollard 1987; Ernst *et al.* 2001; Gudmundsson 2003; Cartwright and Hansen 2006; Schofield *et al.* 2012*a, b*). Sills in the study area consist of mafic gabbro and diabase of similar mineralogical composition to the basalt surrounding horizon H7 (i.e. plagioclase feldspar, pyroxene, olivine, ilmenite and magnetite: Ma *et al.* 2013, 2017), implying that the former fed the latter. This inference is supported by the mapping of sills, dykes, and lava fans and flows as conjoined features. The presence of lava fans implies that basaltic eruptions in the study area were effusive, indicating fissure eruptions (Fedotov 1978) rather than the Hawaiian or Strombolian styles. The cooling and solidification of lava flows

can form multiple lobes, resulting in a complex pattern of ridges and valleys (e.g. Willcock *et al.* 2013; Pedersen *et al.* 2017).

The cross-cutting relationships between sills and the strike-slip fault imply that Sill 2 formed later than the fault, while Sill 1 may have formed earlier than the fault (Fig. 16). Thus, Sill 1 is likely to be older than Sill 2. The relative emplacement sequence of other sills can be inferred from their truncation and cross-cutting relationships (Fig. 12). Sills 2 and 3 exhibit an 'X-type' junction. Sill 2 cuts across the host strata, while Sill 3 follows a relatively weak stratal interface; Sill 2 is likely to have been intruded first, before the relatively weak stratal interface had been exploited by Sill 3 (cf. Ji et al. 2020). The 'U-type' junction between sills 3 and 5 suggests that Sill 5 is younger than Sill 3, and Sill 3 is likely to have acted as a feeder for the formation of Sill 5. The 'T-type' junction between sills 1 and 3 implies that Sill 1 may have acted as the feeder for Sill 3, which grew by bidirectional lateral propagation from the tip of Sill 1 along a weak stratal interface. Thus, the observed sill intersection relationships imply that sills 1, 2, 3 and 5 were progressively younger; this interpretation is not definitive, because sill junction geometries alone are insufficient to determine kinematic models of sill emplacement (Ernst 2014). Sill 6 does

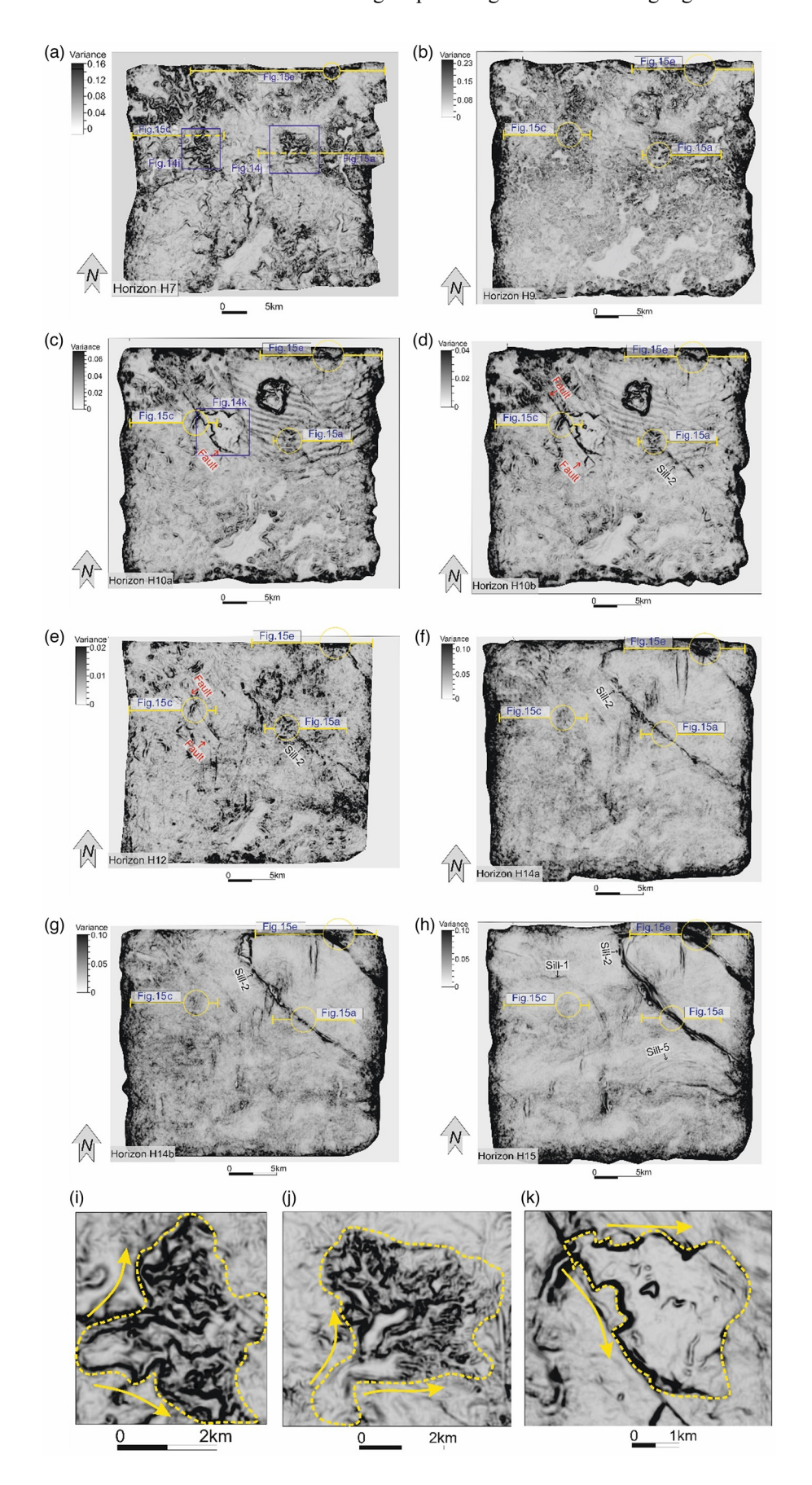


Fig. 14. Variance attribute maps showing the geometry of intrusive rocks and faults at progressively deeper stratigraphic horizons (see Figs 2, 3c and 4b, c): (a) horizon H7; (b) horizon H9; (c) horizon H10a; (d) horizon H10b; (e) horizon H12; (f) horizon H14a; (g) horizon H14b; and (h) horizon H15. (i) and (j) Enlarged maps of fans at horizon H7; the location is shown in (a). (k) Enlarged map of a fan at horizon H10a; the location is shown in Figure 15 are indicated, with circled parts of the cross-sections corresponding to elevated areas and fans in horizon H7.

not intersect other sills but does intrudes into, and is younger than, the volcaniclastic clinoforms below horizon H9 (Figs 4 and 11), which are of lower Permian age (Fig. 2). As described earlier, onlap

of the forced fold above Sill 6 (Fig. 11) indicates that the sill was emplaced prior to the development of horizon H7 during the upper Permian (Fig. 2).

20 X. Dong et al.

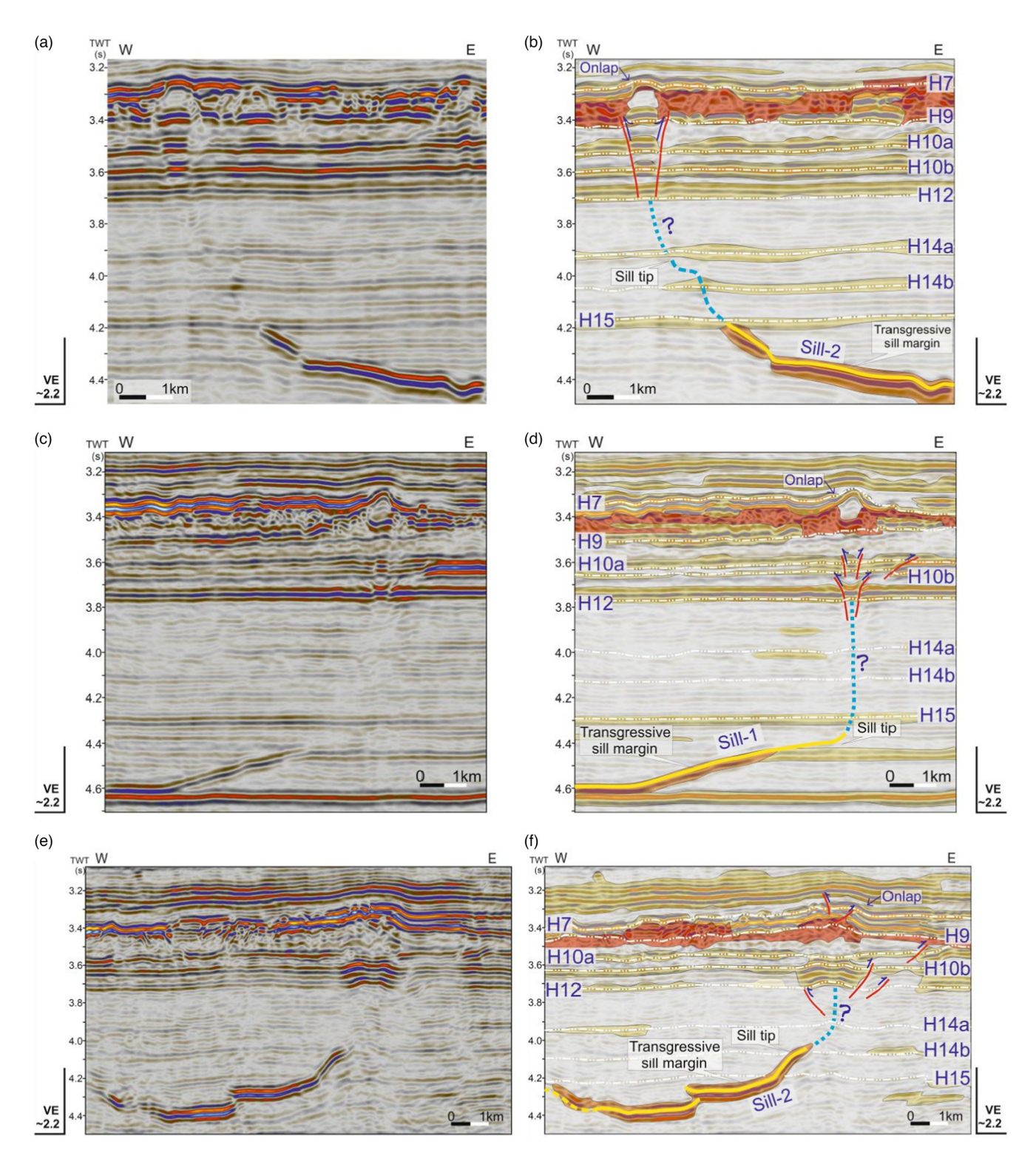


Fig. 15. (a), (c), (e) Uninterpreted and (b), (d), (f) interpreted seismic reflection profiles showing the relationships between intrusive sills and dykes and extrusive volcanic rocks. The locations of the profiles are shown in Figure 14a—h. Interpreted profiles are annotated with seismic facies (summarized in Table 1); faults are shown as solid red lines, sills as solid yellow lines and inferred dykes as blue dashed lines. VE, vertical exaggeration.

Discussion: implications for magma plumbing system

Style and scale of Permian volcanism

The two basalt layers distributed along horizons H7 and H9 indicate relatively gentle, non-explosive eruption of low-viscosity magma, which is normally related to effusive volcanism (La Spina *et al.* 2015). In contrast, the widespread occurrence of dacite and basaltic tuff in the mass transport complex developed

between horizons H7 and H9 indicates a highly explosive eruption (Yang *et al.* 2013) and/or reworking of such eruption products during the lower–middle Permian (Fig. 2). Emplacement of basalt lava flows and associated fans at horizon H7 indicates a return to effusive volcanism via fissure eruptions in the late Permian (Fig. 2).

Permian volcanic rocks are inferred to have covered two-thirds of the Tarim Basin area (Fig. 1a) (Yang *et al.* 2013; Li *et al.* 2014). Our analysis indicates that extrusive volcanic and volcaniclastic rocks have an average thickness of c. 0.2 s TWT (500 m: Figs 3, 4 and 6)

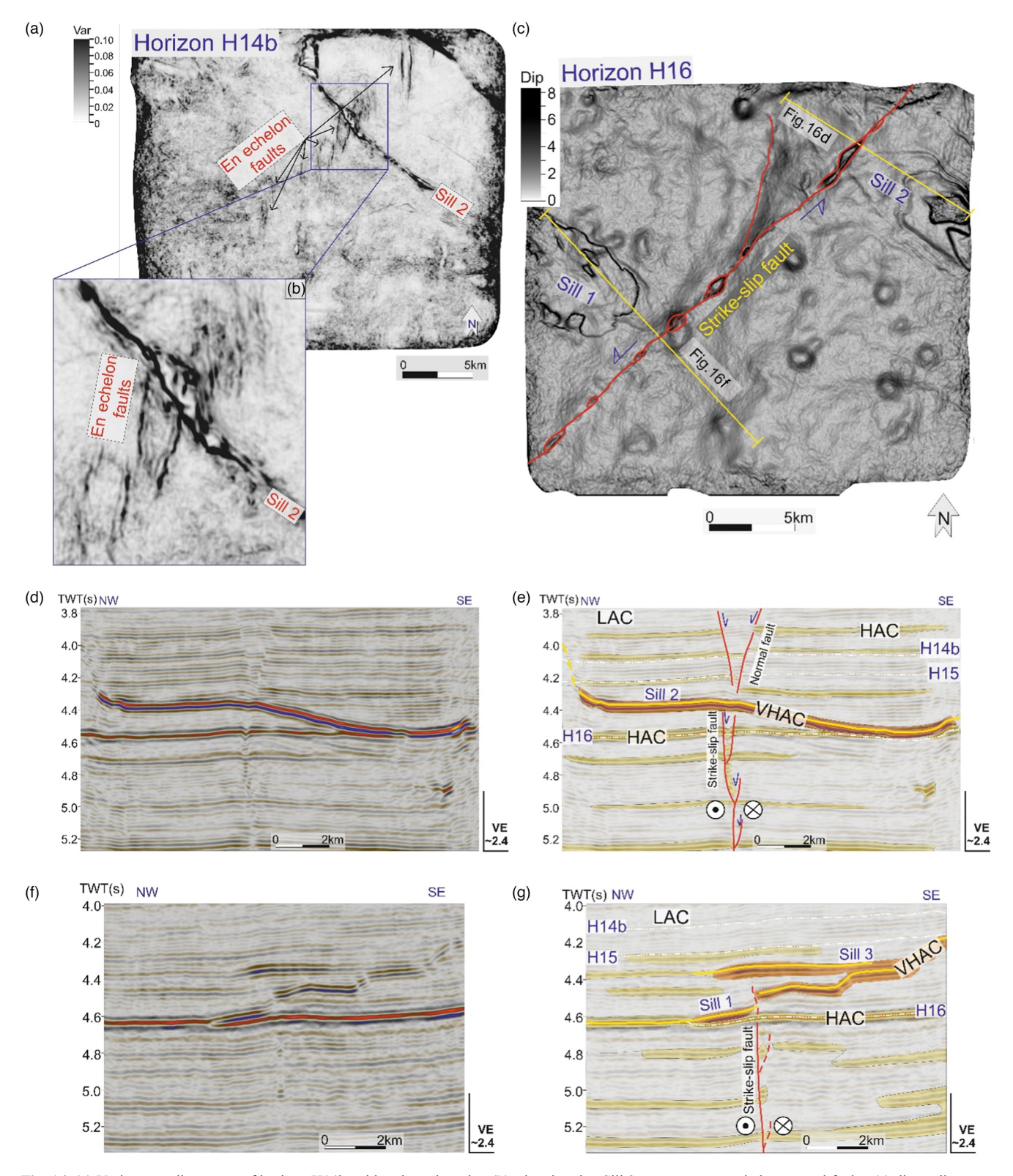


Fig. 16. (a) Variance attribute map of horizon H14b, with enlarged section (b), showing that Sill 2 cuts across en echelon normal faults; (c) dip attribute map of horizon H16, highlighting an SW-NE strike-slip fault and sills 1 and 2 in contact with horizon H16; and (d) and (f) uninterpreted and (e) and (g) interpreted seismic reflection profiles showing cross-cutting relationships between sills 1 and 2 and the strike-slip fault. The profiles are shown in (c). Interpreted profiles are annotated with seismic facies (summarized in Table 1); faults are shown as solid red lines, and sills as solid yellow lines. VE, vertical exaggeration.

in the study area, similar to the thickness of such rocks in the Kalkarindji Continental Flood Basalt Province in Australia (Glass and Phillips 2006) and the Emeishan LIP in southwestern China (Ukstins-Peate and Bryan 2008; Shellnutt 2014). The sills above horizon H16, in upper Ordovician–Permian strata, have a maximum

emplacement depth, estimated as the thickness between horizons H16 and H9, of 2000 m (1 s TWT: Fig. 3b, c), indicating that their feeding source was large and powerful. In addition, the large volume of volcanic and volcaniclastic materials transported as the mass transport complex is consistent with the catastrophic collapse of a

X. Dong et al.

large volcanic centre(s). These local characteristics are consistent with the location of the study area in the Tarim LIP.

Magma composition and source

The source of the intrusive and extrusive igneous rocks is not imaged in the studied seismic data, and lies outside of the study area, but core samples in the Shuntuoguole area (Xiao et al. 2020) indicate that both the intrusive sills and effusive extrusive rocks are mafic in composition (i.e. gabbro and basalt), and the explosive extrusive rocks are intermediate-felsic (i.e. dacite). Continental rifting and mantle plume uplift have both been proposed as possible mechanisms for large-scale volcanism in the Tarim Basin (Yang et al. 2007; Qin et al. 2011; Liu and Leng 2020). Crustal partial melting induced by decompression and water infiltration during continental rifting can lead to the formation of intermediate-felsic magma (Kriegsman 2001), and mantle plume uplift can directly contribute to the formation of mafic-intermediate magma for similar reasons (Campbell and Griffiths 1990). These two geological processes can coincide, as in the modern East African Rift, where continental rifting and mantle plume activity are currently occurring concurrently, and both intermediate and felsic rocks form (Corti 2012; Halldórsson et al. 2014; Koptev et al. 2016). Teleseismic receiver function, electrical conductivity, ambient seismic noise and magnetotelluric data indicate elevated temperatures and electrical conductivity in the upper mantle beneath the Tarim Basin (Vinnik et al. 2018; Guo et al. 2021), together with a dense, highly resistive, high-velocity region in the mid-lower crust associated with localized thinning of the crust and lithosphere beneath the Bachu Uplift (Fig. 1a) (Peng et al. 2024; Qu et al. 2024). These geophysical observations are consistent with the presence of a mantle plume beneath the Tarim Basin (Vinnik et al. 2018; Guo et al. 2021), and plume-related crustal doming and mafic intrusions (dyke swarms?) beneath the Bachu Uplift (Fig. 1a) (Peng et al. 2024; Qu et al. 2024). 3D magnetotelluric inversion of electrical conductivity data from across the Tarim Basin also implies that it is a cratonic rift basin (Zhang et al. 2020). Integration of geochemical and mineral analysis of magma sources, which focus on differentiation and crystallization processes (e.g. Z. Li et al. 2011, 2017; Yang et al. 2013; Xu et al. 2014), with these geophysical results may help to elucidate detailed magma plumbing in the mid-lower crust. In addition, high-resolution seismic tomography (cf. Nataf 2000) and global seismic tomography may be able to image deep lithospheric structures, to further investigate a mantle plume origin.

Strike-slip faults as potential conduits for magma migration

No apparent sills and dykes are imaged beneath horizon H16 (Figs 3, 7, 9, 10, 12, 15 and 16), suggesting that conduits feeding magma to the sills and dykes above horizon H16 are either not imaged or not developed within the study area. One possible interpretation is that the strike-slip fault system below horizon H16 (Fig. 16) acted as a conduit for magma migration, as considered further below. Alternatively, magma may have been intruded laterally into Sill 1 from a feeder that lay beyond the northwestern limit of the study area (Fig. 9) and/or into Sill 2 from a feeder that lay beyond the southeastern limit of the study area (Fig. 10).

Fault zones can provide areas of low stress, facilitating magma migration into weaker interfaces. Magma transport along fault zones occurs typically perpendicular to the least compressive stress (Magee *et al.* 2018; Siregar *et al.* 2019). Dykes aligned along strikeslip faults are documented globally in both outcrop and subsurface, seismically imaged analogues (e.g. Bedard *et al.* 2012; Spacapan *et al.* 2016; Walker 2016; Stephens *et al.* 2017; Siregar *et al.* 2019).

Although no direct evidence of magma in strike-slip fault zones has been found in the study area currently (Liu et al. 2022), similar strike-slip faults are associated with Permian magmatism and mineral deposits at the northwestern margin of the Tarim Basin (Tianshan Folded Belt in Fig. 1a) (Pirajno 2010) and with Permian magmatism-related dolomitization and silicification in the nearby Tazhong Uplift (Fig. 1b) (Wei et al. 2021). Alternatively, magma may have been fed by different sources in nearby areas, potentially along deep-seated strike-slip faults, and then migrated along the unconformity surface H16 to the study area (Gao et al. 2017; Yao et al. 2018; Ji et al. 2020). Our interpretations imply that magma was intruded laterally into Sill 1 from a feeder that lay beyond the northwestern limit of the study area (Fig. 9) and/or into Sill 2 from a feeder that lay beyond the southeastern limit of the study area (Fig. 10).

Reconstruction of the magma plumbing system

Figure 17 summarizes our interpretation of the magma plumbing system in the study area. Gabbro and diabase intrusions were developed between horizons H16 and H9, basalt extrusions occurred along horizons H9 and H7, volcaniclastic shoreline clinoforms were deposited between horizons H10a and H9, and a major volcaniclastic mass transport complex with dacite and basaltic megaclasts developed between horizons H9 and H7. Based on the relationships observed between these components, the evolutionary history of the magma plumbing system is interpreted. Initially, large volumes of volcaniclastic sediment, including dacite tuff, were supplied to feed progradation of shoreline clinoforms (Figs 4 and 5, and labelled ① in Fig. 17). Subsequently, a beddingparallel layer of basalt was emplaced along horizon H9 (Figs 4 and 5, and labelled ② in Fig. 17). The thickness of the basalt layer decreases towards the NE, potentially indicating that it represents lava flows sourced from the SW. Failure of a volcanic slope led to the movement and deposition of a major mass transport complex carrying dacite and basalt megaclasts (Fig. 6 and labelled 3 in Fig. 17). Intrusive volcanism occurred after, and possibly commenced earlier than or during, emplacement of the basalt layers and deposition of the volcaniclastic clinoforms and mass transport complex. Sills were initially intruded along horizon H16 and developed a saucer shape, extending upwards into shallower strata (Fig. 12 and labelled @ in Fig. 17). Some saucer-shaped sills also fed bedding-parallel sills along horizon H15 (Fig. 12 and labelled © in Fig. 15; see also Supplementary Fig. S2). Similarly, these bedding parallel sills also contributed to the formation of further saucer-shaped sills at shallower depths (Fig. 12 and labelled © in Fig. 17; see also Supplementary Fig. S4). Some shallow sills extend upwards into extrusive volcanic strata, resulting in the development of forced folds that deform the volcaniclastic clinoforms and mass transport complex (Fig. 11 and labelled ① in Fig. 17) and fissure vents above the sill tips (Fig. 15 and labelled ® in Fig. 17). As volcanism waned, another basalt layer was emplaced along horizon H7, onlapping the top of the mass transport complex, including the relief generated by forced folds (Fig. 11 and labelled @ in Fig. 17). This basalt layer thins towards the NE, implying that it represents lava flows sourced from the SW, and contains fans fed by the fissure vents above the sill tips (Fig. 14a, i, j).

Although deep-seated strike-slip faults occur below horizon H16 in the study area, there is no direct evidence in the form of dykes to support the hypothesis that magma was transported along these faults to feed sills developed above horizon H16. This absence suggests that the sills may have been fed laterally from a source outside of the study area. Further studies are required in adjacent areas to identify the source(s) of the sills, and their potential relationship to the deep-seated strike-slip faults.

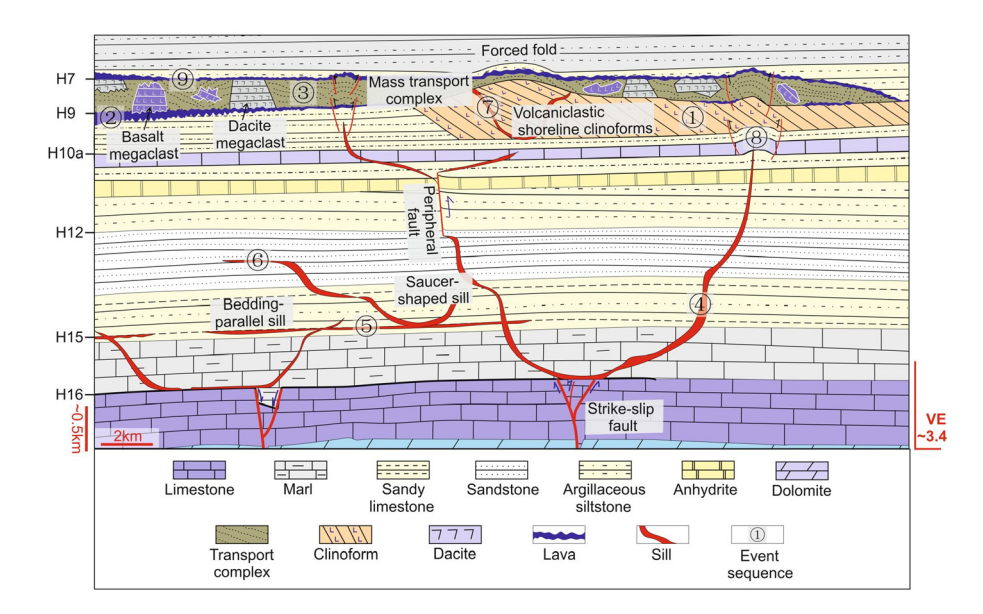


Fig. 17. Geological synthesis model of the magma plumbing system in the study area, and its context within the Tarim LIP. Numbers indicate the relative age of components of the igneous plumbing system ranging from oldest (1) to youngest (9). VE, vertical exaggeration.

Conclusions

3D seismic data calibrated to borehole wireline-logs and published core samples are used to characterize the internal structure, geometry, distribution and interrelationships of igneous rocks and host sedimentary strata in the north-central Tarim Basin. Five seismic facies have been identified: (1) High-Moderate Amplitude Chaotic (HMAC), interpreted as a mass transport complex composed of dacite and basaltic tuff, dacite megaclasts, and basalt megaclasts; (2) Inclined Moderate Amplitude Discontinuous (IMAD), interpreted as a volcaniclastic clinoform set developed along an arcuate, wave-dominated shoreline; (3) Low Amplitude Continuous (LAC), interpreted as host strata; (4) High Amplitude Continuous (HAC), interpreted as basalt, dacite tuff and heterogeneous host strata; and (5) Very High Amplitude Continuous (VHAC) seismic facies, interpreted as gabbro and diabase sills.

These seismic facies are arranged in units that define uppercrustal intrusive and extrusive components of a magma plumbing system. The volcaniclastic clinoform set (IMAD seismic facies) is c. 40 m thick and records c. 10 km of progradation, indicating a high supply of sediment rich in dacite tuff during the earliest volcanism. Overlying this is a high-volume (>250 km³) volcaniclastic mass transport complex (HMAC seismic facies), which contains dacite (LAC seismic facies) and basalt (HAC seismic facies) megaclasts. Water escape during emplacement of the mass transport complex resulted in the formation of large polygonal ridges and depressions (up to 1000 m in lateral spacing and 40 m in relief) at its base. The complex thins toward the NE, indicating transport from the SW, possibly associated with the collapse of a volcanic edifice.

Large, apparently saucer-shaped sills (VHAC seismic facies) are pervasive throughout the 2 km-thick succession of upper Ordovician–middle Permian strata. The termination and crosscutting relationships of the sills indicate the sequence of their intrusion, while subtly thickened peripheral lobes and geometrical steps in some sills indicate their growth directions. The shallowest sill is associated with forced folding of the volcaniclastic clinoforms and mass transport complex. The surface relief of the forced fold is onlapped by a northeastward-thinning basalt layer (HAC seismic facies) that is associated with fissure vents and fans fed by the tips of some shallow, saucer-shaped sills. This basalt layer constitutes the youngest evidence of volcanism in the study area.

Our results document both intrusive and extrusive volcanic rocks, and the spatial and temporal relationships between them, in the central Tarim Basin for the first time. They provide evidence of both effusive and explosive volcanic extrusion, and reworking of significant volumes of volcaniclastic material in previously unrecognized shoreline deposits and mass transport complexes, and thus contribute to our broader understanding of the Tarim LIP.

Scientific editing by Dhananjai Pandey

Acknowledgements We are grateful to Sinopec as sponsors of the Resource Geophysics Academy at Imperial College London for supporting this research. We thank Schlumberger Ltd for provision of Petrel seismic and well interpretation software via an academic software donation. Dr Joyce Neilson and Dr Rebecca Bell are thanked for providing invaluable discussions and comments on the early manuscript. Dr Bo Lin and Dr Chongyang Xiao from the company Sinopec NW are thanked for invaluable discussions on the dataset. The constructive review and editorial comments of Dr Dhananjai Pandey and two anonymous reviewers greatly improved the manuscript.

Author contributions XD: conceptualization (equal), investigation (lead), writing – original draft (lead), writing – review & editing (supporting); GJH: conceptualization (equal), supervision (lead), writing – review & editing (lead); CM: conceptualization (equal), supervision (supporting), writing – review & editing (supporting); LL: conceptualization (equal), supervision (equal), writing – review & editing (supporting); YW: conceptualization (supporting), funding acquisition (lead), supervision (supporting), writing – review & editing (supporting).

Funding This work was funded by Sinopec via their sponsorship of the Resource Geophysics Academy at Imperial College London.

Competing interests The authors declare that they have no known competing financial interests or personal relationships that could have appeared to influence the work reported in this paper.

Data availability All data generated or analysed during this study are included in this published article (and, if present, its supplementary information files).

References

Abdelmalak, M.M., Planke, S., Faleide, J.I., Jerram, D.A., Zastrozhnov, D., Eide, S. and Myklebust, R. 2016. The development of volcanic sequences at rifted margins: new insights from the structure and morphology of the Vøring Escarpment, mid-Norwegian Margin. *Journal of Geophysical Research: Solid Earth*, 121, 5212–5236, https://doi.org/10.1002/2015JB012788

Bedard, J., Naslund, H. *et al.* 2012. Fault-mediated melt ascent in a Neoproterozoic continental flood basalt province, the Franklin sills, Victoria Island, Canada. *Geological Society of America Bulletin*, **124**, 723–736, https://doi.org/10.1130/B30450.1

Berndt, C., Jacobs, C., Evans, A., Gay, A., Elliott, G., Long, D. and Hitchen, K. 2012. Kilometre-scale polygonal seabed depressions in the Hatton Basin, NE

24

- Atlantic Ocean: Constraints on the origin of polygonal faulting. *Marine Geology*, **332**, 126–133, https://doi.org/10.1016/j.margeo.2012.09.013
- Berton, F., Vesely, F.F., Guedes, C.F.C., Souza, M.C. and Angulo, R.J. 2021. Subsurface geomorphology of wave-dominated nearshore deposits: Contrasting styles of reservoir heterogeneity in response to shoreline trajectory. *Marine and Petroleum Geology*, **124**, https://doi.org/10.1016/j.marpetgeo.2020.104821
- Bromley, R.G., Bruun-Petersen, J. and Perch-Nielsen, K. 1970. Preliminary results of mapping in the Palaeozoic and Mesozoic sediments of Scoresby Land and Jameson Land. *Rapport Grønlands Geologiske Undersøgelse*, 30, 17–30, https://doi.org/10.34194/rapggu.v30.7241
- Campbell, I.H. and Griffiths, R.W. 1990. Implications of mantle plume structure for the evolution of flood basalts. *Earth and Planetary Science Letters*, 99, 79–93, https://doi.org/10.1016/0012-821X(90)90072-6
- Cartwright, J. and Hansen, D.M. 2006. Magma transport through the crust via interconnected sill complexes. *Geology*, **34**, 929–932, https://doi.org/10.1130/
- Chen, H., Yang, S., et al. 2006. Sedimentary response to the Early–Mid Permian basaltic magmatism in the Tarim plate. Geology in China, 33, 545–552.
- Chen, J. and Xu, Y. 2021. Permian Large Igneous Provinces and their paleoenvironmental effects. American Geophysical Union Geophysical Monograph Series, 255, 417–434, https://doi.org/10.1002/9781119507444.ch18
- Clairmont, R., Kolawole, F., Omale, A.P. and Bedle, H. 2021. Controls of preexisting structures on clinoform architecture and the associated progradational system elements. *Basin Research*, 33, 875–902, https://doi.org/10.1111/bre. 12487
- Coffin, M.F. and Eldholm, O. 1994. Large igneous provinces: Crustal structure, dimensions, and external consequences. *Reviews of Geophysics*, 32, 1–36, https://doi.org/10.1029/93RG02508
- Corfield, R.I., Carmichael, S., Bennett, J., Akhter, S., Fatimi, M. and Craig, T. 2010. Variability in the crustal structure of the West Indian Continental Margin in the Northern Arabian Sea. *Petroleum Geoscience*, **16**, 257–265, https://doi.org/10.1144/1354-079309-902
- Corti, G. 2012. Evolution and characteristics of continental rifting: Analog modeling-inspired view and comparison with examples from the East African rift system. *Tectonophysics*, **522**, 1–33, https://doi.org/10.1016/j.tecto.2011. 06.010
- Cross, N.E., Williams, Z.K., Jamankulov, A., Bostic, C.E., Gayadeen, V.C., Torrealba, H.J. and Drayton, E.S. 2015. The dynamic behavior of shallow marine reservoirs: Insights from the Pliocene of offshore North Trinidad. AAPG Bulletin, 99, 555–583, https://doi.org/10.1306/09181413165
- Dalley, R.M., Gevers, E.A., Stampfli, G.B., Davies, D.J., Gastaldi, C.N. and Ruitjenberg, P.A. 1989. Dip and azimuth displays for 3D seismic interpretation. *First Break*, 7, 86–95, https://doi.org/10.3997/1365-2397. 2007031
- Deng, S., Li, H., Zhang, Z., Zhang, J. and Yang, X. 2019. Structural characterization of intracratonic strike-slip faults in the central Tarim Basin. AAPG Bulletin, 103, 109–137, https://doi.org/10.1306/06071817354
- Deng, S., Zhao, R., Kong, Q., Li, Y. and Li, B. 2022. Two distinct strike-slip fault networks in the Shunbei area and its surroundings, Tarim Basin: Hydrocarbon accumulation, distribution, and controlling factors. *AAPG Bulletin*, **106**, 77–102, https://doi.org/10.1306/07202119113
- Di Traglia, F., Nolesini, T., Solari, L., Ciampalini, A., Frodella, W., Steri, D. and Casagli, N. 2018. Lava delta deformation as a proxy for submarine slope instability. *Earth and Planetary Science Letters*, **488**, 46–58, https://doi.org/10.1016/j.epsl.2018.01.038
- Dong, X., Hampson, G.J., Lonergan, L. and Wang, Y. 2024. Seismic attribute-driven analysis of an ultra-deep carbonate reservoir: Middle Cambrian to Middle Ordovician strata, north-central Tarim Basin, northwest China. *Journal of Sedimentary Research*, 94, 871–894, https://doi.org/10.2110/jsr. 2023 088
- Eide, C.H., Schofield, N., Jerram, D.A. and Howell, J.A. 2017. Basin-scale architecture of deeply emplaced sill complexes: Jameson Land, East Greenland. *Journal of the Geological Society, London*, **174**, 23–40, https://doi.org/10.1144/jgs2016-018
- Eide, C.H., Schofield, N., Lecomte, I., Buckley, S.J. and Howell, J.A. 2018. Seismic interpretation of sill complexes in sedimentary basins: implications for the sub-sill imaging problem. *Journal of the Geological Society, London*, 175, 193–209, https://doi.org/10.1144/jgs2017-096
- Ernst, R.E. 2014. Large Igneous Provinces. Cambridge University Press, Cambridge, UK, https://doi.org/10.1017/CBO9781139025300
- Ernst, R.E., Grosfils, E.B. and Moge, D. 2001. Giant dike swarms: Earth, Venus, and Mars. *Annual Review of Earth and Planetary Sciences*, 29, 489–534, https://doi.org/10.1146/annurev.earth.29.1.489
- Ernst, R.E., Liikane, D.A., Jowitt, S.M., Buchan, K.L. and Blanchard, J.A. 2019. A new plumbing system framework for mantle plume-related continental Large Igneous Provinces and their mafic–ultramafic intrusions. *Journal of Volcanology and Geothermal Research*, 384, 75–84, https://doi.org/10.1016/j.jvolgeores.2019.07.007
- Fedotov, S.A. 1978. Ascent of basic magmas in the crust and the mechanism of basaltic fissure eruptions. *International Geology Review*, 20, 33–48, https://doi.org/10.1080/00206817809471367
- Francis, E.H. 1982. Emplacement mechanism of late Carboniferous tholeite sills in northern Britain. *Journal of the Geological Society, London*, **139**, 1–20, https://doi.org/10.1144/gsjgs.139.1.0001

- Galland, O., Planke, S., Neumann, E.R. and Malthe-Sørenssen, A. 2009. Experimental modelling of shallow magma emplacement: Application to saucer-shaped intrusions. *Earth and Planetary Science Letters*, 277, 373–383, https://doi.org/10.1016/j.epsl.2008.11.003
- https://doi.org/10.1016/j.epsl.2008.11.003
 Gao, Z., Tian, W., Wang, L., Shi, Y. and Pan, M. 2017. Emplacement of intrusions of the Tarim Flood Basalt Province and their impacts on oil and gas reservoirs: A 3D seismic reflection study in Yingmaili fields, Tarim Basin, northwest China. *Interpretation*, 5, SK51–SK63, https://doi.org/10.1190/INT-2016-0165.1
- Glass, L.M. and Phillips, D. 2006. The Kalkarindji continental flood basalt province: A new Cambrian large igneous province in Australia with possible links to faunal extinctions. *Geology*, 34, 461–464, https://doi.org/10.1130/ G22122.1
- Goulty, N. and Schofield, N. 2008. Implications of simple flexure theory for the formation of saucer-shaped sills. *Journal of Structural Geology*, 30, 812–817, https://doi.org/10.1016/j.jsg.2008.04.002
- Greenfield, L., Millett, J.M., Howell, J., Jerram, D.A., Watton, T., Healy, D. and Planke, S. 2020. The 3D facies architecture and petrophysical properties of hyaloclastite delta deposits: An integrated photogrammetry and petrophysical study from southern Iceland. *Basin Research*, 32, 1081–1104, https://doi.org/ 10.1111/bre.12415
- Gudmundsson, A. 2003. Surface stresses associated with arrested dykes in rift zones. *Bulletin of Volcanology*, 65, 606–619, https://doi.org/10.1007/s00445-003-0289-7
- Guest, J.E. and Sánchez, R.J. 1969. A large dacitic lava flow in northern Chile. Bulletin Volcanologique, 33, 778–790, https://doi.org/10.1007/BF02596749
- Guo, F., Yang, D., Eriksson, K.A. and Guo, L. 2015. Paleoenvironments, stratigraphic evolution and reservoir characteristics of the Upper Cretaceous Yingjisha Group, southwest Tarim Basin. *Marine and Petroleum Geology*, 67, 336–355, https://doi.org/10.1016/j.marpetgeo.2015.05.023
- Guo, J., Lian, X. and Wang, X. 2021. Electrical conductivity evidence for the existence of a mantle plume beneath Tarim Basin. *Applied Sciences*, 11, 893, https://doi.org/10.3390/app11030893
- Halldórsson, S.A., Hilton, D.R., Scarsi, P., Abebe, T. and Hopp, J. 2014. A common mantle plume source beneath the entire East African Rift System revealed by coupled helium–neon systematics. *Geophysical Research Letters*, 41, 2304–2311, https://doi.org/10.1002/2014GL059424
- Hansen, D.M., Cartwright, J.A. and Thomas, D. 2004. 3D seismic analysis of the geometry of igneous sills and sill junction relationships. *Geological Society*, *London, Memoirs*, 29, 199–208, https://doi.org/10.1144/GSL.MEM.2004. 029.01.19
- Hodgson, D.M., Brooks, H.L., Ortiz-Karpf, A., Spychala, Y., Lee, D.R. and Jackson, C.A.L. 2018. Entrainment and abrasion of megaclasts during submarine landsliding and their impact on flow behaviour. *Geological Society, London, Special Publications*, 477, 223–240, https://doi.org/10.1144/ SP477.26
- Holford, S.P., Schofield, N., Jackson, C.A.L., Magee, C., Green, P.F. and Duddy, I.R. 2013. Impacts of igneous intrusions on source and reservoir potential in prospective sedimentary basins along the Western Australian continental margins. In: Keep, M. and Moss, S.J. (eds) West Australian Basins Symposium. Proceedings of the Petroleum Exploration Society of Australia Symposium, Perth, Western Australia. Petroleum Exploration Society of Australia (PESA), Perth, Australia, 1–12.
- Hu, W. 2019. Research on seismic identification and description technology of Permian igneous in central Tarim Basin: take Shunbei area as an example. *Progress in Geophysics*, 34, 1434–1440, https://doi.org/10.6038/pg2019CC0502
- Ismaiel, M., Krishna, K.S., Srinivas, K., Mishra, J. and Saha, D. 2017. Internal structure of the 85°E ridge, Bay of Bengal: Evidence for multiphase volcanism. *Marine and Petroleum Geology*, 80, 254–264, https://doi.org/10. 1016/j.marpetgeo.2016.11.020
- Jackson, C.A.L., Grunhagen, H., Howell, J.A., Larsen, A.L., Andersson, A., Boen, F. and Groth, A. 2010. 3D seismic imaging of lower delta-plain beach ridges: lower Brent Group, northern North Sea. *Journal of the Geological Society, London*, 167, 1225–1236, https://doi.org/10.1144/0016-76492010-053
- Ji, T., Yang, W., Pu, R., Wu, X. and Wu, X. 2020. Analysis of vertical position relationships between igneous sills and an unconformity surface – Interpretation of seismic profiles from the Northern Tarim Basin, NW China. *Interpretation*, 8, T739–T752, https://doi.org/10.1190/INT-2019-0129.1
- Johnson, A.M. and Pollard, D.D. 1973. Mechanics of growth of some laccolithic intrusions in the Henry mountains, Utah, I: Field observations, Gilbert's model, physical properties and flow of the magma. *Tectonophysics*, 18, 261–309, https://doi.org/10.1016/0040-1951(73)90050-4
- Joppen, M. and White, R.S. 1990. The structure and subsidence of Rockall Trough from two-ship seismic experiments. *Journal of Geophysical Research: Solid Earth*, **95**, 19 821–19 837, https://doi.org/10.1029/ JB095iB12p19821
- Kim, J.R., Lin, S.Y. and Oh, J.W. 2022. The survey of lava tube distribution in Jeju Island by multi-source data fusion. *Remote Sensing*, 14, 443, https://doi. org/10.3390/rs14030443
- Koptev, A., Burov, E., Calais, E., Leroy, S., Gerya, T., Guillou-Frottier, L. and Cloetingh, S. 2016. Contrasted continental rifting via plume–craton interaction: Applications to Central East African Rift. Geoscience Frontiers, 7, 221–236, https://doi.org/10.1016/j.gsf.2015.11.002

- Koson, S., Chenrai, P. and Choowong, M. 2013. Seismic attributes and their applications in seismic geomorphology. *Bulletin of Earth Sciences of Thailand*, 6, 1–9.
- Kriegsman, L.M. 2001. Partial melting, partial melt extraction and partial back reaction in anatectic migmatites. *Lithos*, **56**, 75–96, https://doi.org/10.1016/ S0024-4937(00)00060-8
- Lan, X., Lü, X., Zhu, Y., Yu, H., Zhou, J. and Zhu, F. 2014. Characteristics and differential accumulation of oil/gas in Lower Paleozoic marine carbonate on northern slope of Tazhong Low Rise, Tarim Basin, NW China: a case study of Lower Ordovician Yingshan Formation. *Arabian Journal of Geosciences*, 7, 4487–4498, https://doi.org/10.1007/s12517-013-1091-2
- La Spina, G., Burton, M. and Vitturi, M.D.M. 2015. Temperature evolution during magma ascent in basaltic effusive eruptions: a numerical application to Stromboli volcano. *Earth and Planetary Science Letters*, 426, 89–100, https://doi.org/10.1016/j.epsl.2015.06.015
- Lebedeva-Ivanova, N., Polteau, S., Bellwald, B., Planke, S., Berndt, C. and Stokke, H.H. 2018. Toward one-meter resolution in 3D seismic. *The Leading Edge*, 37, 818–828, https://doi.org/10.1190/tle37110818.1
- Li, D., Yang, S., Chen, H., Cheng, X., Li, K., Jin, X. and Zou, S. 2014. Late Carboniferous crustal uplift of the Tarim plate and its constraints on the evolution of the Early Permian Tarim Large Igneous Province. *Lithos*, 204, 36–46, https://doi.org/10.1016/j.lithos.2014.05.023
- Li, D., Chang, J., Qiu, N., Wang, J., Zhang, M., Wu, X. and Ma, A. 2022. The thermal history in sedimentary basins: a case study of the central Tarim Basin, Western China. *Journal of Asian Earth Sciences*, 229, https://doi.org/10.1016/ i.iseaes.2022.105149
- Li, H., Lü, H. and Pu, R. 2017. LA-ICP-MS zircon U-Pb age of dykes from central Tarim Basin and its geological significance. *Geological Bulletin of China*, 36, 1010–1021, https://doi.org/10.12097/gbc.dztb-36-6-1010
- Li, K., Lv, H.L., Pu, R. and Cao, Z. 2016. Relationships among volcanic and hydrothermal activity and faults from the Shunnan 3-D well zone in the Tadong Area (Tarim Basin, China). *Arabian Journal of Geosciences*, **9**, 1–18, https://doi.org/10.1007/s12517-016-2685-2
- Li, X., Chang, H. et al. 2023. Reconstruction of the proto-type basin and tectonopaleogeography of Tarim Block in the Mesozoic. Frontiers in Earth Science, 11, https://doi.org/10.3389/feart.2023.1121428
- Li, Z., Chen, H., Song, B., Li, Y., Yang, S. and Yu, X. 2011. Temporal evolution of the Permian large igneous province in Tarim Basin in northwestern China. *Journal of Asian Earth Sciences*, 42, 917–927, https://doi.org/10.1016/j. jseaes.2011.05.009
- Li, Z., Li, Y., Zou, S., Sun, H. and Li, D. 2017. The temporospatial characteristics and magma dynamics of the Early Permian Tarim Large Igneous Province. Bulletin of Mineralogy, Petrology and Geochemistry, 36, 418–431.
- Li, Z., Yang, Z. et al. 2020. Three-dimensional seismic exploration method for ultra-deep fault-related dissolution reservoirs in the Shunbei desert area. Geophysical Prospecting for Petroleum, 59, 283–294, https://doi.org/10. 3969/j.issn.1000-1441.2020.02.015
- Lin, C., Li, H. and Liu, J. 2012. Major unconformities, tectonostratigraphic framework, and evolution of the superimposed Tarim Basin, Northwest China. *Journal of Earth Science*, **23**, 395–407, https://doi.org/10.1007/s12583-012-0263-4
- Liu, C., Zhang, L., Guo, J. and Wang, M. 2012. Application of sequence stratigraphy to Triassic terrestrial strata in Tahe area of Tarim Basin. *Journal of Central South University*, 19, 1388–1398, https://doi.org/10.1007/s11771-012-1155-6
- Liu, H. and Leng, W. 2020. Tarim Large Igneous Province caused by a wide and wet mantle plume. *Journal of Geophysical Research: Solid Earth*, 125, e2019JB019001, https://doi.org/10.1029/2019JB019001
- Liu, X., Guan, P., Pan, W.Q., Tian, W., Huang, S.Y., Pan, Y. and Yu, H.J. 2011. Meticulous characterization of Permian volcanic rocks' spatial distribution and its geological significance in the Tarim Basin. *Acta Scientiarum Naturalium Universitatis Pekinensis*, 47, 315–320, https://xbna.pku.edu.cn/ EN/Y2011/V47/I2/315
- Liu, Y., Deng, S., Zhang, R., Liu, J., Huang, C. and Gao, T. 2022. Characterization and petroleum geological significance of deep igneous intrusions and related structures in the Shunbei area, Tarim Basin. *Oil and Gas Geology*, 43, 105–117.
- Lonergan, L.C., Borlandelli, A., Taylor, M.Q. and Flanagan, K. 2007. The three dimensional geometry of sandstone injection complexes in the Gryphon Field, United Kingdom North Sea. AAPG Memoirs, 87, 103–112, https://doi.org/10. 1306/1209854M873260
- Ma, Q., Liao, Z. and Tang, Z. 2017. The discovery of the Late Ordovician zircon U–Pb dating in Tarim Basin. Geology in China, 44, 1251–1252, https://doi. org/10.12029/gc20170614
- Ma, Z., Ren, L., Huang, W. and Yue, X. 2013. Basic characteristics of igneous rock in the middle area of Tarim Basin. Special Oil and Gas Reservoirs, 20, 64–67.
- Magee, C., Bastow, I.D., De Vries, B.V.W., Jackson, C.A.L., Hetherington, R., Hagos, M. and Hoggett, M. 2017. Structure and dynamics of surface uplift induced by incremental sill emplacement. *Geology*, 45, 431–434, https://doi. org/10.1130/G38839.1
- Magee, C., Stevenson, C.T.E. et al. 2018. Magma plumbing systems: a geophysical perspective. *Journal of Petrology*, 59, 1217–1251, https://doi.org/ 10.1093/petrology/egy064
- Magee, C., Ernst, R.E., Muirhead, J., Phillips, T. and Jackson, C.A.L. 2019.Magma transport pathways in Large Igneous Provinces: lessons from

- combining field observations and seismic reflection data. *In*: Srivastava, R.K., Ernst, R.E. and Peng, P. (eds) *Dyke Swarms of the World: A Modern Perspective*. Springer, Singapore, 45–85, https://doi.org/10.1007/978-981-13-1666-1_2
- Maharjan, D., Planke, S. et al. 2024. Rapid loading and deformation of soft sediments during emplacement of a lava delta in the Vøring Basin, Mid-Norwegian Margin. Geological Society, London, Special Publications, 547, 465–482, https://doi.org/10.1144/SP547-2023-43
- Malthe-Sørenssen, A., Planke, S., Svensen, H. and Jamtveit, B. 2004. Formation of saucer-shaped sills. *Geological Society, London, Special Publications*, 234, 215–227, https://doi.org/10.1144/GSL.SP.2004.234.01.13
- Moscardelli, L., Wood, L. and Mann, P. 2006. Mass-transport complexes and associated processes in the offshore area of Trinidad and Venezuela. AAPG Bulletin, 90, 1059–1088, https://doi.org/10.1306/02210605052
- Nataf, H.C. 2000. Seismic imaging of mantle plumes. Annual Review of Earth and Planetary Sciences, 28, 391–417, https://doi.org/10.1146/annurev.earth. 28 1 391
- Niu, Y., Han, J. et al. 2024. Igneous rock intrusions in the western Shunbei area, Tarim Basin: characteristics and coupling relationships with faults. Oil & Gas Geology, 45, 231–242, https://doi.org/10.11743/ogg20240116
- Nwoko, J., Kane, I. and Huuse, M. 2020. Mass transport deposit (MTD) relief as a control on post-MTD sedimentation: Insights from the Taranaki Basin, offshore New Zealand. *Marine and Petroleum Geology*, 120, https://doi.org/ 10.1016/j.marpetgeo.2020.104489
- Ogiesoba, O.C., Klokov, A. and Hernandez, R. 2015. Diffraction imaging of polygonal faults within a submarine volcanic terrain, Maverick Basin, South Texas. *Interpretation*, **3**, SF81–SF99, https://doi.org/10.1190/INT-2014-0105.1
- Olierook, H.K.H., Timms, N.E., Merle, R.E., Jourdan, F. and Wilkes, P.G. 2015. Paleodrainage and fault development in the southern Perth Basin, Western Australia during and after the breakup of Gondwana from 3D modelling of the Bunbury Basalt. *Australian Journal of Earth Sciences*, 62, 289–305, https://doi.org/10.1080/08120099.2015.1030774
- Pedersen, G.B.M., Höskuldsson, A. *et al.* 2017. Lava field evolution and emplacement dynamics of the 2014–2015 basaltic fissure eruption at Holuhraun, Iceland. *Journal of Volcanology and Geothermal Research*, **340**, 155–169, https://doi.org/10.1016/j.jvolgeores.2017.02.027
- Pedersen, G.K., Larsen, L.M., Pedersen, A.K. and Hjortkjær, B.F. 1998. The synvolcanic Naajaat lake, Paleocene of West Greenland. *Palaeogeography*, *Palaeoclimatology*, *Palaeoecology*, **140**, 271–287, https://doi.org/10.1016/S0031-0182(98)00034-0
- Peng, M., Tan, H. et al. 2024. N–S variations of crustal structure beneath the central Tarim Basin from joint inversion of receiver functions, ambient seismic noise surface wave dispersion, and magnetotelluric data. *Tectonophysics*, 877, https://doi.org/10.1016/j.tecto.2024.230299
- Pirajno, F. 2010. Intracontinental strike-slip faults, associated magmatism, mineral systems and mantle dynamics: examples from NW China and Altay-Sayan (Siberia). *Journal of Geodynamics*, 50, 325–346, https://doi.org/10. 1016/j.jog.2010.01.018
- Planke, S., Alvestad, E. and Eldholm, O. 1999. Seismic characteristics of basaltic extrusive and intrusive rocks. *The Leading Edge*, 18, 342–348, https://doi.org/ 10.1190/1.1438289
- Planke, S., Rasmussen, T., Rey, S.S. and Myklebust, R. 2005. Seismic characteristics and distribution of volcanic intrusions and hydrothermal vent complexes in the Vøring and Møre basins. Geological Society, London, Petroleum Geology Conference Series, 6, 833–844, https://doi.org/10.1144/ 0060833
- Planke, S., Millett, J.M., Maharjan, D., Jerram, D.A., Abdelmalak, M.M., Groth, A. and Myklebust, R. 2017. Igneous seismic geomorphology of buried lava fields and coastal escarpments on the Vøring volcanic rifted margin. *Interpretation*, 5, 161–177, https://doi.org/10.1190/INT-2016-0164.1
- Pollard, D. 1987. Elementary fracture mechanics applied to the structural interpretation of dykes. *Geological Association of Canada Special Papers*, 34, 5–24.
- Polteau, S., Mazzini, A., Galland, O., Planke, S. and Malthe-Sørenssen, A. 2008. Saucer-shaped intrusions: Occurrences, emplacement and implications. *Earth and Planetary Science Letters*, 266, 195–204, https://doi.org/10.1016/j.epsl. 2007.11.015
- Pu, R., Zhang, Y. and Luo, J. 2012. Seismic reflection, distribution, and potential trap of Permian volcanic rocks in the Tahe field. *Journal of Earth Science*, 23, 421–430, https://doi.org/10.1007/s12583-012-0265-2
- Qi, L. 2023. Technical demand and innovative application of geophysical exploration technology for marine ultra-deep carbonate rocks in Shunbei area, Tarim Basin. *Geophysical Prospecting for Petroleum*, 62, 381–394, https://doi.org/10.12431/issn.1000-1441.2023.62.03.001
- Qin, K., Su, B. et al. 2011. SIMS zircon U–Pb geochronology and Sr–Nd isotopes of Ni–Cu-bearing mafic–ultramafic intrusions in eastern Tianshan and Beishan in correlation with flood basalts in Tarim Basin (NW China): Constraints on a ca. 280 Ma mantle plume. American Journal of Science, 311, 237–260, https://doi.org/10.2475/03.2011.03
- Qu, C., Shen, X., Yu, C., Liang, X. and Yang, W. 2024. A study of Mesozoic– Cenozoic tectonic evolution of the Tarim Basin with S-wave receiver functions. *Geological Journal*, **59**, 2139–2155, https://doi.org/10.1002/gj. 4987

- Quirie, A.K., Schofield, N., Hartley, A., Hole, M.J., Archer, S.G., Underhill, J.R. and Holford, S.P. 2019. The Rattray Volcanics: Mid-Jurassic fissure volcanism in the UK Central North Sea. *Journal of the Geological Society, London*, 176, 462–481, https://doi.org/10.1144/jgs2018-151
- Rickwood, P.C. 1990. The anatomy of a dyke and the determination of propagation and, magma flow directions. *In*: Parker, A.J., Rickwood, P.C. and Tucker, D.H. (eds) *Mafic Dykes and Emplacement Mechanisms*. Balkema, Rotterdam, The Netherlands, 81–100.
- Rider, M.H. and Kennedy, M. 2011. The Geological Interpretation of Well Logs. 3rd edn. Rider-French Consulting Ltd, Edinburgh.
- Sato, H., Fujii, T. and Nakada, S. 1992. Crumbling of dacite dome lava and generation of pyroclastic flows at Unzen volcano. *Nature*, 360, 664–666, https://doi.org/10.1038/360664a0
- Sauro, F., Pozzobon, R., Massironi, M., De Berardinis, P., Santagata, T. and De Waele, J. 2020. Lava tubes on Earth, Moon and Mars: A review on their size and morphology revealed by comparative planetology. *Earth-Science Reviews*, 209, https://doi.org/10.1016/j.earscirev.2020.103288
- Schofield, N.J., Brown, D.J., Magee, C. and Stevenson, C.T. 2012a. Sill morphology and comparison of brittle and non-brittle emplacement mechanisms. *Journal of the Geological Society, London*, 169, 127–141, https://doi. org/10.1144/0016-76492011-078
- Schofield, N.J., Heaton, L., Holford, S.P., Archer, S.G., Jackson, C.A.L. and Jolley, D.W. 2012b. Seismic imaging of 'broken bridges': linking seismic to outcrop-scale investigations of intrusive magma lobes. *Journal of the Geological Society, London*, 169, 421–426, https://doi.org/10.1144/0016-76492011-150
- Schofield, N.J., Holford, S.P., Millett, J., Brown, D., Jolley, D., Passey, S.R. and Stevenson, C.T. 2017. Regional magma plumbing and emplacement mechanisms of the Faroe–Shetland Sill Complex: implications for magma transport and petroleum systems within sedimentary basins. *Basin Research*, 29, 41–63, https://doi.org/10.1111/bre.12164
- Shangguan, S.M., Tian, W., Xu, Y.G., Guan, P. and Pan, L. 2012. The eruption characteristics of the Tarim Flood Basalt. *Acta Petrologica Sinica*, 28, 1261–1272.
- Shellnutt, J. 2014. The Emeishan large igneous province: A synthesis. Geoscience Frontiers, 5, 369–394, https://doi.org/10.1016/j.gsf.2013.07.003
- Siregar, E., Omosanya, K.O., Magee, C. and Johansen, S.E. 2019. Impacts of fault-sill interactions on sill emplacement in the Vøring Basin, Norwegian North Sea. *Journal of Structural Geology*, 126, 156–174, https://doi.org/10. 1016/j.jsg.2019.06.006
- Skogeid, J., Pedersen, T., Eldholm, O. and Larsen, B. 1992. Tectonism and magmatism during the NE Atlantic continental break-up: the Vøring margin. *Geological Society, London, Special Publications*, 68, 305–320, https://doi. org/10.1144/GSL.SP.1992.068.01.19
- Smallwood, J.R. and Maresh, J. 2002. The properties, morphology and distribution of igneous sills: modelling, borehole data and 3D seismic from the Faroe–Shetland area. *Geological Society, London, Special Publications*, 197, 271–306, https://doi.org/10.1144/GSL.SP.2002.197.01.11
- Smellie, J.L., Wilch, T.I. and Rocchi, S. 2013. 'A'ā lava-fed deltas: A new reference tool in paleoenvironmental studies. *Geology*, 41, 403–406, https:// doi.org/10.1130/G33631.1
- Spacapan, J.B., Galland, O., Leanza, H.A. and Planke, S. 2016. Control of strikeslip fault on dyke emplacement and morphology. *Journal of the Geological Society, London*, 173, 573–576, https://doi.org/10.1144/jgs2015-166
- Srivastava, R.K., Ernst, R.E., Buchan, K.L. and De Kock, M. 2022. An overview of the plumbing systems of large igneous provinces and their significance. *Geological Society, London, Special Publications*, 518, 1–16, https://doi.org/ 10.1144/SP518-2021-167
- Stephens, T.L., Walker, R.J., Healy, D., Bubeck, A., England, R.W. and McCaffrey, K.J. 2017. Igneous sills record far-field and near-field stress interactions during volcano construction: Isle of Mull, Scotland. Earth and Planetary Science Letters, 478, 159–174, https://doi.org/10.1016/j.epsl.2017. 09.003
- Sun, Q., Jackson, C.A.L., Magee, C., Mitchell, S.J. and Xie, X. 2019. Extrusion dynamics of deepwater volcanoes revealed by 3-D seismic data. *Solid Earth*, 10, 1269–1282, https://doi.org/10.5194/se-10-1269-2019
- Sun, Q., Fan, T., Gao, Z., Wu, J., Zhang, H., Jiang, Q. and Yuan, Y. 2021. New insights on the geometry and kinematics of the Shunbei 5 strike-slip fault in the central Tarim Basin, China. *Journal of Structural Geology*, 150, https://doi. org/10.1016/j.jsg.2021.104400
- Tang, L., Huang, T. et al. 2014. Fault systems and their mechanisms of the formation and distribution of the Tarim Basin, NW China. Journal of Earth Science, 25, 169–182, https://doi.org/10.1007/s12583-014-0410-1
- Thomson, K. 2007. Determining magma flow in sills, dykes and laccoliths and their implications for sill emplacement mechanisms. *Bulletin of Volcanology*, **70**, 183–201, https://doi.org/10.1007/s00445-007-0131-8
- Tian, W., Campbell, I.H., Allen, C.M., Guan, P., Pan, W., Chen, M. and Zhu, W. 2010. The Tarim picrite–basalt–rhyolite suite, a Permian flood basalt from northwest China with contrasting rhyolites produced by fractional crystallization and anatexis. *Contributions to Mineralogy and Petrology*, 160, 407–425, https://doi.org/10.1007/s00410-009-0485-3
- Tian, W., Li, X. and Wang, L. 2021. Forced fold amplitude and sill thickness constrained by wireline and 3-D seismic data suggest an elastic magmainduced deformation in Tarim Basin, NW China. *Minerals*, 11, 293, https://doi.org/10.3390/min11030293

- Tomasi, I., Massironi, M., Meyzen, C.M., Pozzobon, R., Sauro, F., Penasa, L. and Martinez-Frias, J. 2022. Inception and evolution of La Corona lava tube system (Lanzarote, Canary Islands, Spain). *Journal of Geophysical Research: Solid Earth*, **127**, e2022JB024056, https://doi.org/10.1029/2022JB024056
- Ukstins-Peate, I. and Bryan, S.E. 2008. Re-evaluating plume-induced uplift in the Emeishan large igneous province. *Nature Geoscience*, 1, 625–629, https://doi. org/10.1038/ngeo281
- Vinnik, L., Deng, Y., Kosarev, G., Oreshin, S. and Makeyeva, L. 2018. Permian plume beneath Tarim from receiver functions. *Solid Earth*, 9, 1179–1185, https://doi.org/10.5194/se-9-1179-2018
- Walker, F., Schofield, N., Millett, J., Jolley, D., Hole, M. and Stewart, M. 2022. Paleogene volcanic rocks in the northern Faroe–Shetland Basin and Møre Marginal High: understanding lava field stratigraphy. *Geological Society*, *London, Special Publications*, 495, 199–235, https://doi.org/10.1144/SP495-2019-13
- Walker, R.J. 2016. Controls on transgressive sill growth. Geology, 44, 99–102, https://doi.org/10.1130/G37144.1
- Wang, L., Tian, W., Shi, Y. and Guan, P. 2015. Volcanic structure of the Tarim flood basalt revealed through 3-D seismological imaging. Science Bulletin, 60, 1448–1456, https://doi.org/10.1007/s11434-015-0866-0
- Wang, T. and Liu, J. 1991. A preliminary investigation on formative phase and rifting of Tarim Basin. In: Jia, R. (ed.) Research of Petroleum Geology of Northern Tarim Basin. China University of Geoscience Press, Wuhan, China, 115–124.
- Wang, T., Jin, Z., Shi, Z., Dai, X. and Cheng, R. 2020. Phanerozoic plate history and structural evolution of the Tarim Basin, northwestern China. *International Geology Review*, 62, 1555–1569, https://doi.org/10.1080/00206814.2019. 1661038
- Ward, N.I., Alves, T.M. and Blenkinsop, T.G. 2018. Submarine sediment routing over a blocky mass-transport deposit in the Espírito Santo Basin, SE Brazil. *Basin Research*, 30, 816–834, https://doi.org/10.1111/bre.12282
- Watt, W.S. and Watt, M. 1971. Preliminary report of the mapping of the basalts of parts of Milne Land and Gåseland. *Rapport Grønlands Geologiske Undersøgelse*, **37**, 42–50, https://doi.org/10.34194/rapggu.v37.7274
- Wei, D., Gao, Z., Fan, T., Niu, Y. and Guo, R. 2021. Volcanic events-related hydrothermal dolomitisation and silicification controlled by intra-cratonic strike-slip fault systems: Insights from the northern slope of the Tazhong Uplift, Tarim Basin, China. *Basin Research*, 33, 2411–2434, https://doi.org/ 10.1111/bre.12562
- Wei, X., Xu, Y.G., Feng, Y.X. and Zhao, J.X. 2014. Plume–lithosphere interaction in the generation of the Tarim large igneous province, NW China: geochronological and geochemical constraints. *American Journal of Science*, 314, 314–356, https://doi.org/10.2475/01.2014.09
- Willcock, M.A.W., Cas, R.A.F., Giordano, G. and Morelli, C. 2013. The eruption, pyroclastic flow behaviour, and caldera in-filling processes of the extremely large volume (>1290 km³), intra-to extra-caldera, Permian Ora (Ignimbrite) Formation, Southern Alps, Italy. *Journal of Volcanology and Geothermal Research*, 265, 102–126, https://doi.org/10.1016/j.jvolgeores. 2013.08.012
- Wright, K.A., Davies, R.J., Jerram, D.A., Morris, J.E. and Fletcher, R. 2012. Application of seismic and sequence stratigraphic concepts to a lava-fed delta system in the Faroe–Shetland Basin, UK and Faroes. *Basin Research*, 24, 91–106, https://doi.org/10.1111/j.1365-2117.2011.00513.x
- Wu, N., Jackson, C.A.L., Johnson, H.D., Hodgson, D.M., Clare, M.A., Nugraha, H.D. and Li, W. 2021. The formation and implications of giant blocks and fluid escape structures in submarine lateral spreads. *Basin Research*, 33, 1711–1730, https://doi.org/10.1111/bre.12532
- Xiao, C., Yang, L., Lin, B. and You, D. 2020. Volcanic activity stages and distribution during the Permian in the Shunbei area, Tarim Basin. *Petroleum Geology and Experiment*, 42, 177–185, https://doi.org/10.11781/ sysydz202002177
- Xu, K., Yu, B., Gong, H., Ruan, Z., Pan, Y. and Ren, Y. 2015. Carbonate reservoirs modified by magmatic intrusions in the Bachu area, Tarim Basin, NW China. Geoscience Frontiers, 6, 779–790, https://doi.org/10.1016/j.gsf. 2015.02.002
- Xu, X., Chen, Q., Chu, C., Li, G., Liu, C. and Shi, Z. 2017. Tectonic evolution and paleokarstification of carbonate rocks in the Paleozoic Tarim Basin. *Carbonates and Evaporites*, 32, 487–496, https://doi.org/10.1007/s13146-016-0307-4
- Xu, Y., Wei, X., Luo, Z., Liu, H. and Cao, J. 2014. The Early Permian Tarim Large Igneous Province: Main characteristics and a plume incubation model. *Lithos*, 204, 20–35, https://doi.org/10.1016/j.lithos.2014.02.015
- Yang, J., Zhu, W., Guan, D., Zhu, B., Yuan, L., Xiang, X. and Wu, X. 2016. 3D seismic interpretation of subsurface eruptive centers in a Permian large igneous province, Tazhong Uplift, central Tarim Basin, NW China. *International Journal of Earth Sciences*, 105, 2311–2326, https://doi.org/10.1007/s00531-015-1289-5
- Yang, S.F., Li, Z., Chen, H., Santosh, M., Dong, C.W. and Yu, X. 2007. Permian bimodal dyke of Tarim Basin, NW China: Geochemical characteristics and tectonic implications. *Gondwana Research*, 12, 113–120, https://doi.org/10. 1016/j.gr.2006.10.018
- Yang, S.F., Chen, H., Li, Z., Li, Y., Yu, X., Li, D. and Meng, L. 2013. Early Permian Tarim Large Igneous Province in northwest China. Science China Earth Sciences, 56, 2015–2026, https://doi.org/10.1007/s11430-013-4653-y

- Yao, Z. 2024. Spatial and temporal distribution of igneous sills in the central Tarim Basin and their geological implications. *Minerals*, 14, 862, https://doi. org/10.3390/min14090862
- Yao, Z., He, G., Li, C.F. and Dong, C. 2018. Sill geometry and emplacement controlled by a major disconformity in the Tarim Basin, China. *Earth and Planetary Science Letters*, 501, 37–45, https://doi.org/10.1016/j.epsl.2018.08. 026
- Yilmaz, Ö. 2001. Seismic Data Analysis: Processing, Inversion, and Interpretation of Seismic Data. 2nd edn. Investigations in Geophysics Series, 10. Society of Exploration Geophysicists, Tulsa, OK, https://doi.org/ 10.1190/1.9781560801580
- Yu, X., Yang, S.F., Chen, H.L., Chen, Z.Q., Li, Z.L., Batt, G.E. and Li, Y.Q. 2011. Permian flood basalts from the Tarim Basin, northwest China: SHRIMP zircon U–Pb dating and geochemical characteristics. *Gondwana Research*, 20, 485–497, https://doi.org/10.1016/j.gr.2010.11.009
- Zhang, L., Zhao, C., Yu, P., Xiang, Y., Peng, X., Koyama, T. and Yang, W. 2020. The electrical conductivity structure of the Tarim basin in NW China as revealed by three-dimensional magnetotelluric inversion. *Journal of Asian Earth Sciences*, 187, https://doi.org/10.1016/j.jseaes.2019.104093

- Zhang, Y., Liu, J. and Guo, Z. 2010. Permian basaltic rocks in the Tarim basin, NW China: Implications for plume–lithosphere interaction. *Gondwana Research*, **18**, 596–610, https://doi.org/10.1016/j.gr.2010.03.006
- Zhou, M., Zhao, J., Jiang, C., Gao, J., Wang, W. and Yang, S. 2009. OIB-like, heterogeneous mantle sources of Permian basaltic magmatism in the western Tarim Basin, NW China: Implications for a possible Permian large igneous province. *Lithos*, 113, 583–594, https://doi.org/10.1016/j.lithos.2009.06.027
- Zhu, G. and Zhang, K.J. 2022. Did the eruption of the Tarim LIP control the formation of Paleozoic hydrocarbon reservoirs in the Tarim Basin, China? Gondwana Research, 101, 224–232, https://doi.org/10.1016/j.gr.2021.08.007
- Zhu, G., Su, J. et al. 2013. Formation mechanisms of secondary hydrocarbon pools in the Triassic reservoirs in the northern Tarim Basin. Marine and Petroleum Geology, 46, 51–66, https://doi.org/10.1016/j.marpetgeo.2013.06. 006
- Zimmer, E.H., Howell, J.A., Schofield, N. and Gawthorpe, R.L. 2019. Seismic geomorphology linked to sequence stratigraphy of an Eocene delta in the Outer Moray Firth, UKCS. *Marine and Petroleum Geology*, **104**, 150–167, https://doi.org/10.1016/j.marpetgeo.2019.03.014